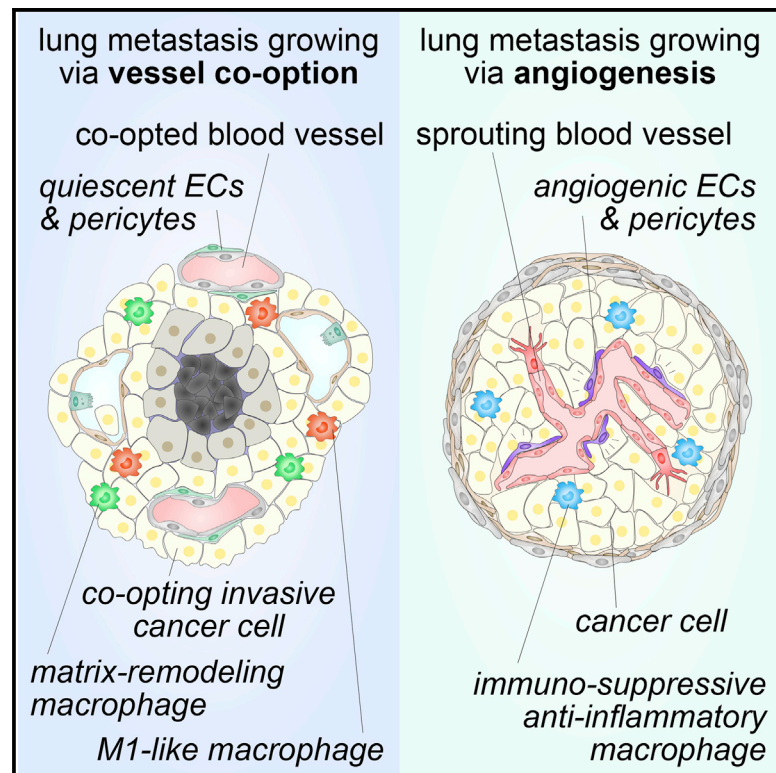# Cell Reports

Tumor vessel co-option probed by single-cell analysis

Graphical abstract

Authors

Laure-Anne Teuwen,
Laura P.M.H. De Rooij, Anne Cuypers, ...,
Yonglun Luo, Peter Vermeulen,
Peter Carmeliet

Correspondence

alun@biomed.au.dk (Y.L.),
peter.carmeliet@kuleuven.be (P.C.)

In brief

Teuwen et al. report a single-cell transcriptome study comprising >30,000 cells from a lung-vessel co-option tumor model. They find that co-opted tumor endothelial cells and pericytes transcriptionally resemble their healthy counterparts and identify macrophage and cancer-cell subtypes involved in vessel co-option.

Highlights

- Single-cell RNA-seq of 31,964 cells from a lung-vessel co-option tumor model

- The transcriptome of co-opted and healthy vascular cells is largely similar

- Matrix-remodeling macrophages might assist invasive cancer cells to co-opt vessels

- An M1-like macrophage subtype may keep vascular cells quiescent

CellPress

Cell Reports

Article

Tumor vessel co-option probed by single-cell analysis

Laure-Anne Teuwen,[1,2,3] Laura P.M.H. De Rooij,[1] Anne Cuypers,[1] Katerina Rohlenova,[1,12] Sébastien J. Dumas,[1] Melissa García-Caballero,[1,13] Elda Meta,[1] Jacob Amersfoort,[1] Federico Taverna,[1] Lisa M. Becker,[1] Nuphar Veiga,[1] Anna Rita Cantelmo,[1,14] Vincent Geldhof,[1] Nadine V. Conchinha,[1] Joanna Kalucka,[1,15] Lucas Treps,[1] Lena-Christin Conradi,[1,16] Shawez Khan,[1,17] Tobias K. Karakach,[1,18,19] Stefaan Soenen,[4] Stefan Vinckier,[1] Luc Schoonjans,[1,5] Guy Eelen,[1] Steven Van Laere,[2,3] Mieke Dewerchin,[1] Luc Dirix,[2,3] Massimiliano Mazzone,[6] Yonglun Luo,[7,8,9,10,*] Peter Vermeulen,[2,3] and Peter Carmeliet[1,5,11,20,*]

[1]Laboratory of Angiogenesis and Vascular Metabolism, Center for Cancer Biology (CCB), VIB, Department of Oncology, Leuven Cancer Institute, KU Leuven, Leuven 3000, Belgium
[2]Translational Cancer Research Unit, GZA Hospitals Sint-Augustinus, Antwerp 2610, Belgium
[3]Center for Oncological Research, University of Antwerp, Antwerp 2000, Belgium
[4]NanoHealth and Optical Imaging Group, Department of Imaging and Pathology, KU Leuven, Leuven 3000, Belgium
[5]State Key Laboratory of Ophthalmology, Zhongshan Ophthalmic Center, Sun Yat-Sen University, 510275, Guangzhou, Guangdong, P.R. China
[6]Laboratory of Tumor Inflammation and Angiogenesis, CCB, VIB, Department of Oncology, Leuven Cancer Institute, KU Leuven, Leuven 3000, Belgium
[7]Department of Biomedicine, Aarhus University, Aarhus 8000, Denmark
[8]Lars Bolund Institute of Regenerative Medicine, BGI-Qingdao, Qingdao 266555, P.R. China
[9]BGI-Shenzhen, Shenzhen 518083, China
[10]China National GeneBank, BGI-Shenzhen, Shenzhen 518120, P.R. China
[11]Laboratory of Angiogenesis and Vascular Heterogeneity, Department of Biomedicine, Aarhus University, Aarhus 8000, Denmark
[12]Present address: Institute of Biotechnology of the Czech Academy of Sciences, Praha – západ 252 50, Central Bohemia, Czechia
[13]Present address: Department of Molecular Biology and Biochemistry, Faculty of Sciences, and IBIMA (Biomedical Research Institute of Málaga), University of Málaga, Andalucía Tech, 29071 Málaga, Spain
[14]Present address: Laboratory of Cell Physiology, INSER MU1003, Lille University, Villeneuve d'Ascq 59655, France
[15]Present address: Aarhus Institute of Advanced Studies (AIAS); Department of Biomedicine, Aarhus University, Aarhus DK-8000, Denmark
[16]Present address: Clinic of General, Visceral and Pediatric Surgery, University Medical Center Göttingen, Göttingen 37077, Germany
[17]Present address: National Center for Cancer Immune Therapy (CCIT-DK), Department of Oncology, Copenhagen University Hospital, Herlev 2730, Denmark
[18]Present address: Bioinformatics Core Laboratory, Children's Hospital Research Institute of Manitoba, Winnipeg, MB 3RE 3P4, Canada
[19]Present address: Rady Faculty of Health Sciences, Department of Pediatrics and Child Health, University of Manitoba, Winnipeg MB R3A 1S1, Manitoba Canada
[20]Lead contact
*Correspondence: alun@biomed.au.dk (Y.L.), peter.carmeliet@kuleuven.be (P.C.)
https://doi.org/10.1016/j.celrep.2021.109253
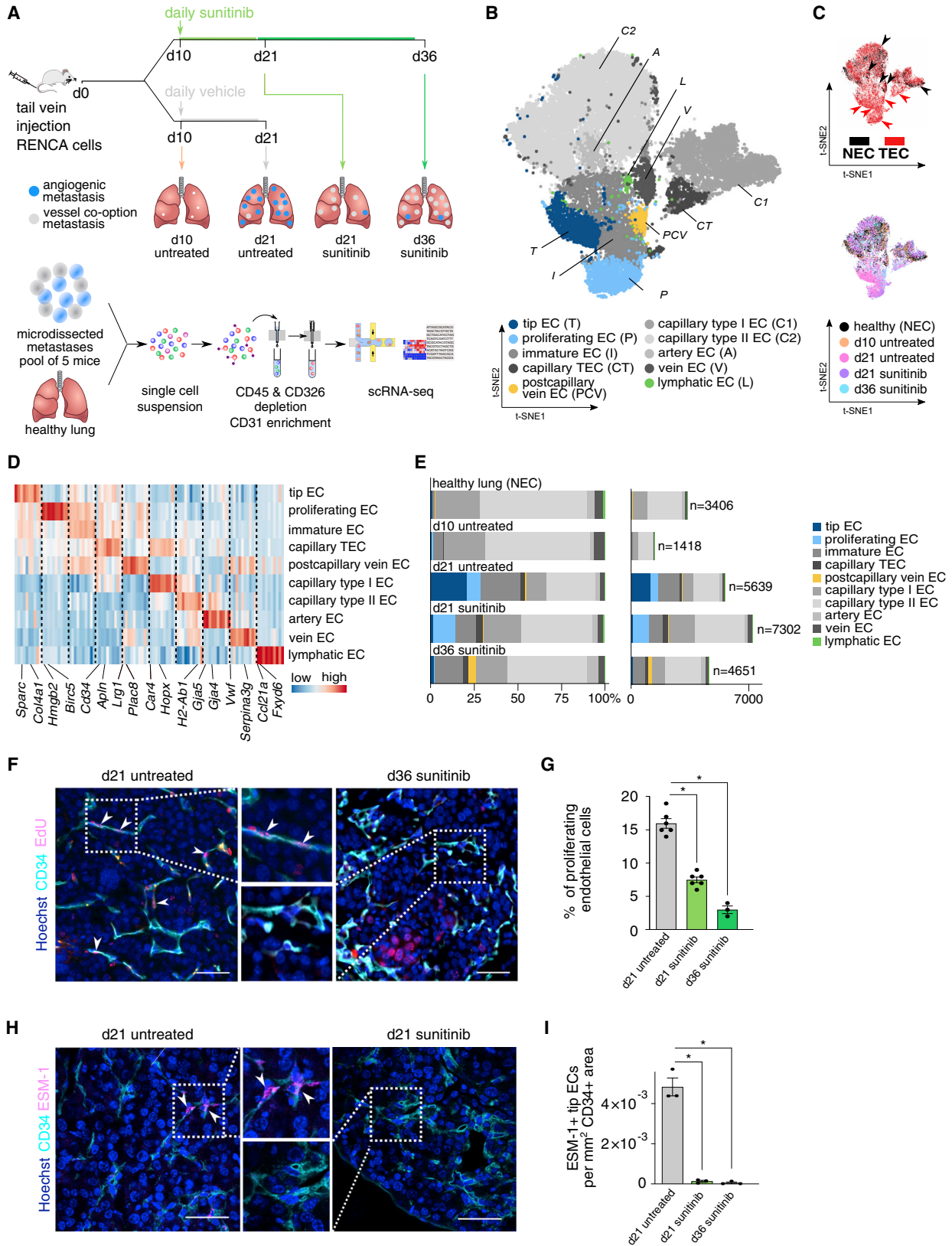
SUMMARY

Tumor vessel co-option is poorly understood, yet it is a resistance mechanism against anti-angiogenic therapy (AAT). The heterogeneity of co-opted endothelial cells (ECs) and pericytes, co-opting cancer and myeloid cells in tumors growing via vessel co-option, has not been investigated at the single-cell level. Here, we use a murine AAT-resistant lung tumor model, in which VEGF-targeting induces vessel co-option for continued growth. Single-cell RNA sequencing (scRNA-seq) of 31,964 cells reveals, unexpectedly, a largely similar transcriptome of co-opted tumor ECs (TECs) and pericytes as their healthy counterparts. Notably, we identify cell types that might contribute to vessel co-option, i.e., an invasive cancer-cell subtype, possibly assisted by a matrix-remodeling macrophage population, and another M1-like macrophage subtype, possibly involved in keeping or rendering vascular cells quiescent.

INTRODUCTION

Many tumors establish a vascular supply via vessel sprouting (commonly referred to as angiogenesis), which has been widely studied and has become a target for anti-angiogenic therapy (AAT) (Carmeliet and Jain, 2011). However, tumors can also grow and invade the surrounding parenchymal tissue via alternative vascularization mechanisms, including vessel co-option (Carmeliet and Jain, 2011). In this process, cancer cells "hijack" pre-existing blood vessels to grow and invade healthy tissue (Donnem et al., 2018; Kuczynski et al., 2019). Vessel co-option occurs frequently in primary and metastatic tumors and is often

A daily sunitinib

tail vein injection RENCA cells

angiogenic metastasis
vessel co-option metastasis

d10 untreated
d21 untreated
d21 sunitinib
d36 sunitinib

microdissected metastases pool of 5 mice

healthy lung

single cell suspension

CD45 & CD326 depletion CD31 enrichment

scRNA-seq

B

tip EC (T)
proliferating EC (P)
immature EC (I)
capillary TEC (CT)
postcapillary vein EC (PCV)
capillary type I EC (C1)
capillary type II EC (C2)
artery EC (A)
vein EC (V)
lymphatic EC (L)

C

NEC   TEC

healthy (NEC)
d10 untreated
d21 untreated
d21 sunitinib
d36 sunitinib

D

tip EC
proliferating EC
immature EC
capillary TEC
postcapillary vein EC
capillary type I EC
capillary type II EC
artery EC
vein EC
lymphatic EC

low   high

Sparc *Col4a1* *Hmgb2* *Birc5* *Cd34* *Apln* *Lrg1* *Plac8* *Car4* *Hopx* *H2-Ab1* *Gja5* *Gja4* *Vwf* *Serpina3g* *Ccl21a* *Fxyd6*

E

healthy lung (NEC)   n=3406
d10 untreated   n=1418
d21 untreated   n=5639
d21 sunitinib   n=7302
d36 sunitinib   n=4651

tip EC
proliferating EC
immature EC
capillary TEC
postcapillary vein EC
capillary type I EC
capillary type II EC
artery EC
vein EC
lymphatic EC

F

d21 untreated   d36 sunitinib

Hoechst CD34 EdU

G

% of proliferating endothelial cells

d21 untreated
d21 sunitinib
d36 sunitinib

H

d21 untreated   d21 sunitinib

Hoechst CD34 ESM-1

I

ESM-1+ tip ECs per mm² CD34+ area

d21 untreated
d21 sunitinib
d36 sunitinib

(legend on next page)

associated with a worse prognosis (Kuczynski et al., 2019). However, this phenomenon has been poorly studied, and only a handful of molecular mechanisms have been proposed (Donnem et al., 2018; Lucio-Eterovic et al., 2009; Valiente et al., 2014), explaining why there are currently no tangible therapeutic strategies to target vessel co-option.

The cellular heterogeneity in tumors growing via vessel co-option has been minimally studied and only through bulk RNA sequencing (RNA-seq) analysis (Lucio-Eterovic et al., 2009) but not at the single-cell level. However, because vessel co-option often co-exists with vessel sprouting in tumors (Bridgeman et al., 2017; Pezzella et al., 1997) and insufficient marker genes of co-opted tumor endothelial cells (ECs) (TECs) are available to reliably distinguish co-opted from angiogenic ECs, we performed single-cell RNA-seq (scRNA-seq) to distinguish both EC types in silico. Furthermore, it is unknown whether (1) co-opted TECs transcriptionally differ from healthy, normal ECs (NECs); (2) co-opted pericytes adopt a distinct phenotype; and (3) co-opting cancer and immune cells in tumors growing via vessel co-option express different transcriptomic signatures. To address these questions, we performed an exploratory study to characterize the transcriptional phenotypes of the different cell types in tumors growing via vessel co-option at the single-cell level.

Vessel co-option can be induced by VEGF (receptor)-blockade AAT in human colorectal liver metastases and in mouse models of hepatic cell carcinoma, glioma, brain metastases, and renal cancer lung metastases (Kuczynski et al., 2019). In fact, vessel co-option has been proposed to be a mechanism of resistance against VEGF-targeted AAT (Bridgeman et al., 2017; Frentzas et al., 2016; Kuczynski et al., 2016). However, there are <100 publications on vessel co-option, in contrast to the >100,000 publications on vessel sprouting. Because of the clinical importance to unravel the molecular basis of tumor vessel co-option when contributing to the resistance against VEGF-blockade AAT, we focused this study primarily on that process. The primary goal, however, was not to provide a comprehensive single-cell taxonomy of each cell type in tumors growing via vessel co-option; rather, we aimed at identifying cellular phenotypes putatively contributing to tumor vessel co-option.

RESULTS

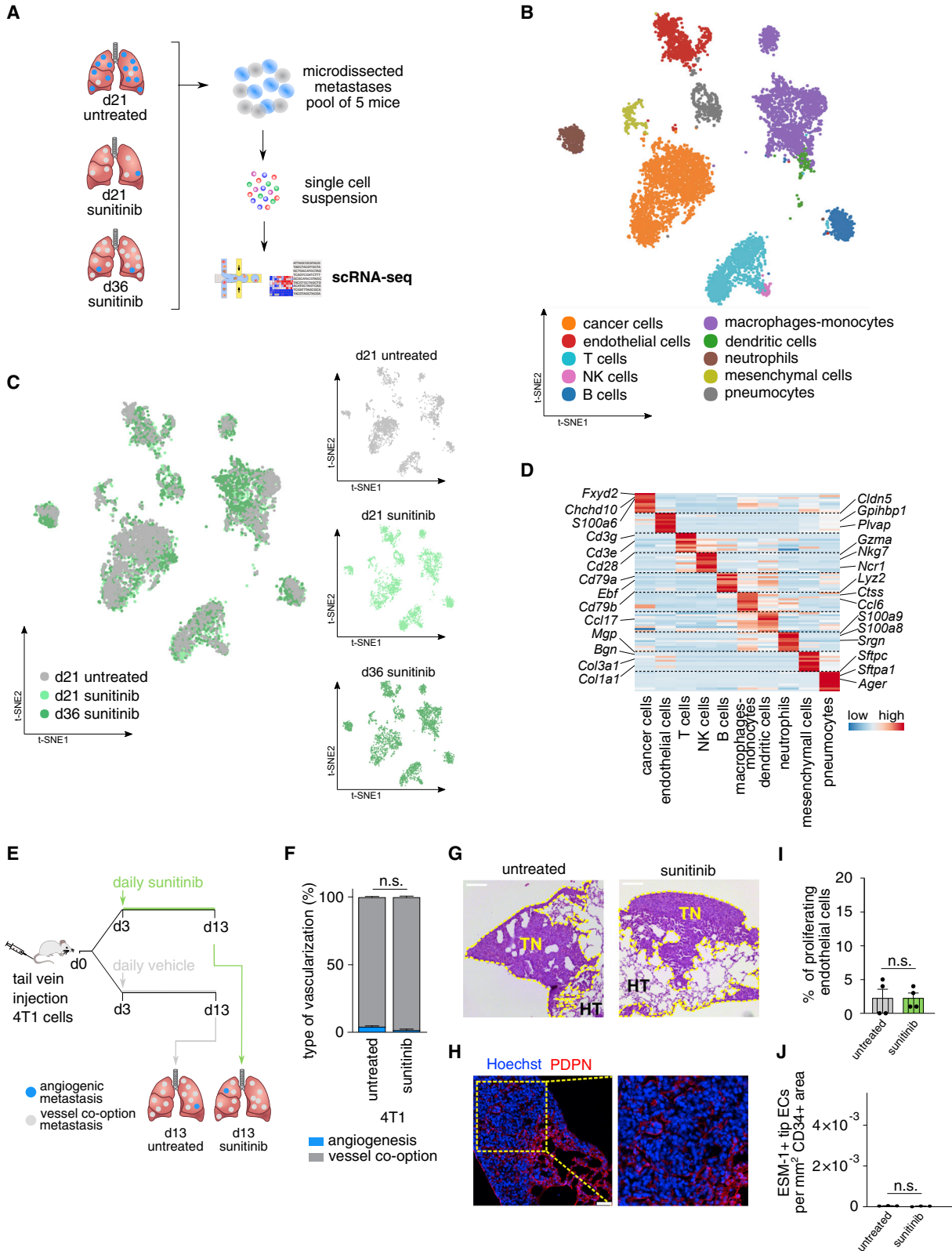### Renal cancer lung metastasis model of vessel co-option

To model vessel co-option induced by VEGF-targeted AAT and to compare vessel co-option with vessel sprouting in a single model, we used a renal cancer lung metastasis mouse model by injecting renal adenocarcinoma (RENCA) cells into the tail vein of syngeneic BALB/c mice (Figure 1A) (Bridgeman et al., 2017). Confirming previous findings (Bridgeman et al., 2017), at day (d) 21 after injection, most metastases (70%) grew via vessel sprouting, characterized by globular, metastatic nodules that excluded healthy alveolar cells, whereas the remaining metastases (30%) grew via vessel co-option, characterized by cancer cells co-opting healthy lung structures in an irregular/infiltrative manner, as quantified by hematoxylin and eosin (H&E) staining and double staining for the EC marker CD31 and the pneumocyte marker PDPN (Figures S1A and S1B). In contrast, at d21 after a 10-day sunitinib treatment, 70% of the metastases grew via vessel co-option, whereas the remaining 30% grew via angiogenesis (Figures 1A and S1B).

Although sunitinib treatment is initially effective in suppressing tumor growth (Figure S1C, three left bars) (Bridgeman et al., 2017), we explored whether prolonged sunitinib treatment (beyond the periods previously tested in this model) would induce resistance and whether continued tumor growth would rely on vessel co-option to obtain a VEGF-blockade-induced tumor-vessel co-option model. Indeed, upon prolonged treatment until d36, metastatic burden increased again, as quantified by H&E staining (Figure S1C, right bar) and bioluminescence imaging (Figure S1D). Untreated tumor-bearing mice could not be followed over this long period because of tumor overload. Under long-term sunitinib treatment, vessel co-option persisted as the predominant vascularization pattern in 75% of the metastatic nodules (Figures S1A and S1B, right bar), revealing that vessel co-option primarily fueled continued metastatic growth under prolonged VEGF-blockade AAT. Because sunitinib inhibits vessel sprouting (Faivre et al., 2007), it also caused hypoxia in metastatic nodules upon long-term treatment (Figures S1E and S1F).

We first explored whether we could distinguish the transcriptome signatures of angiogenic versus co-opted TECs at the single-cell level. Because sufficiently large numbers of sequenced

---

Figure 1. scRNA-seq of ECs from a renal cancer experimental lung metastasis model

(A) Scheme of study design of EC-enriched cohort.

(B) t-SNE plot color-coded for the 10 identified EC subtypes.

(C) t-SNE plots color-coded for ECs from a healthy condition (NEC) and tumor conditions (TEC) (top) or for ECs from each indicated treatment condition (bottom).

(D) Gene expression levels of top-10 marker genes of TEC subtypes. In this and all further heatmaps depicting marker genes, colors represent the following: red, high expression; blue, low expression.

(E) Left, relative composition of EC subtypes in indicated conditions, weighted by the number of cells per condition. Right, absolute composition of EC subtypes in indicated conditions.

(F) Representative images of renal cancer lung metastases, stained for EdU, CD34, and Hoechst (nuclei). Middle images are magnifications of respective boxed areas. Arrowheads, proliferating ECs.

(G) Quantification of the percentage of proliferating ECs in (F).

(H) Representative images of renal cancer lung metastases stained for ESM-1, CD34, and Hoechst (nuclei). Middle images are magnifications of the respective boxed areas. Arrowheads, tip ECs.

(I) Quantification of ESM-1$^+$ ECs per CD34$^+$ area in (H).

Data are means ± SEM; n = 3–6 (G); n = 3 (I); *p < 0.05 by one-way ANOVA with Tukey's multiple comparisons test. Scale bar, 50 μm (F and H).

See Figure S1 and Tables S1, S2, S3, and S4.

A

d21 untreated

d21 sunitinib

d36 sunitinib

microdissected metastases pool of 5 mice

single cell suspension

scRNA-seq

B

- cancer cells
- endothelial cells
- T cells
- NK cells
- B cells
- macrophages-monocytes
- dendritic cells
- neutrophils
- mesenchymal cells
- pneumocytes

t-SNE2

t-SNE1

C

d21 untreated

d21 sunitinib

d36 sunitinib

- d21 untreated
- d21 sunitinib
- d36 sunitinib

t-SNE2

t-SNE1

t-SNE2

t-SNE1

D

Fxyd2, *Chchd10*, *S100a6*, *Cd3g*, *Cd3e*, *Cd28*, *Cd79a*, *Ebf*, *Cd79b*, *Ccl17*, *Mgp*, *Bgn*, *Col3a1*, *Col1a1*

Cldn5, *Gpihbp1*, *Plvap*, *Gzma*, *Nkg7*, *Ncr1*, *Lyz2*, *Ctss*, *Ccl6*, *S100a9*, *S100a8*, *Srgn*, *Sftpc*, *Sftpa1*, *Ager*

cancer cells, endothelial cells, T cells, NK cells, B cells, macrophages-monocytes, dendritic cells, neutrophils, mesenchymal cells, pneumocytes

low high

E

tail vein injection 4T1 cells

daily sunitinib

daily vehicle

d0, d3, d13

d3, d13

d13 untreated

d13 sunitinib

- angiogenic metastasis
- vessel co-option metastasis

F

type of vascularization (%)

n.s.

untreated sunitinib

4T1

- angiogenesis
- vessel co-option

G

untreated

sunitinib

TN

HT

TN

HT

H

Hoechst PDPN

I

% of proliferating endothelial cells

n.s.

untreated sunitinib

J

ESM-1+ tip ECs per mm^2 CD34+ area

$4×10^{-3}$

$2×10^{-3}$

n.s.

untreated sunitinib

(legend on next page)

ECs are required to optimally identify EC phenotypes (Goveia et al., 2020; Kalucka et al., 2020; Rohlenova et al., 2020), we enriched TECs using established methods (magnetic-activated cell sorting of CD45⁻/CD326⁻(EPCAM)/CD31⁺ ECs [Kalucka et al., 2020]) (Figure 1A). We analyzed the following conditions (Figure 1A): mice that did not receive sunitinib treatment at d21 after cancer-cell injection (termed d21 untreated); mice before the onset of sunitinib treatment (d10 untreated; at this time point, metastases were very small [Figures S1C, left bar, and S1G], with an indistinguishable type of vascularization as compared with d21 untreated mice [not shown]); and mice that were treated with sunitinib for a short-term (d21 sunitinib) or long-term (d36 sunitinib) period. For this EC-enriched cohort, we micro-dissected and pooled 60 lung metastases from five mice per study group, used lungs from healthy mice as controls, and generated single-cell suspensions.

Co-opted ECs
NECs from lungs of healthy mice and lung TECs were subjected to scRNA-seq using the 10× Genomics-based single-tube protocol to prepare the libraries. After quality control (Table S1), we *in silico* selected ECs (Figures S1H and S1I; Table S1), performed batch-correction, and used graph-based clustering to group 22,416 high-quality cells into distinct clusters, which we visualized using t-distributed stochastic neighbor embedding (t-SNE) (Figures 1B and 1C; Table S1). Based on the top-50 marker genes (Table S2), known canonical marker genes (Table S3), and previously established gene signatures from in-house-generated lung EC scRNA-seq studies (Goveia et al., 2020; Kalucka et al., 2020), we identified 10 EC phenotypes, of which, five (capillary types 1 and 2, artery, vein, and lymphatic) were represented in both NECs and TECs (though at varying fractions), whereas the remaining five EC phenotypes (tip, proliferating, immature, postcapillary vein, and TEC capillaries) were predominantly detected in TECs (Figures 1B–1E), confirming previous scRNA-seq findings (Goveia et al., 2020).

We recently reported that lung tumors contain heterogeneous TEC phenotypes, including angiogenic TECs (proliferating, tip, and immature TECs) and tumor-specific capillary TECs (Goveia et al., 2020). Comparable to NECs, untreated d10 metastases exhibited few angiogenic EC phenotypes (only some proliferating TECs) (Figure 1E; Table S4), likely because the metastases

were still small and did not require additional vessel sprouting (Figures S1C and S1G). In untreated d21 metastases, substantial numbers of angiogenic (proliferating, tip, and immature) TECs and capillary TECs were detected (Figure 1E; Table S4). Upon prolonged sunitinib treatment, the most angiogenic TECs (tip and proliferating TECs) progressively disappeared (Figure 1E; Table S4). Staining for EdU (proliferation) and ESM-1 (tip cell marker) (Rocha et al., 2014) confirmed these findings (Figures 1F–1I and S1J).

Similar findings were obtained in a repeat cohort, in which we focused on the critical d21 untreated and d21 and d36 sunitinib-treated groups only. In that experiment, we isolated all cell types from the tumor (Figure 2A). Using graph-based clustering, we grouped 9,548 high-quality cells into distinct clusters, which we visualized using t-SNE (Figures 2B and 2C; Table S1). Based on the top 50 marker genes (Table S2) and known canonical marker genes (Table S3), we identified six major cell types: ECs (see above), cancer cells, lymphocytes (T cells, natural killer [NK] cells, and B cells), myeloid cells (monocytes, macrophages, dendritic cells, and neutrophils), mesenchymal cells, and pneumocytes (Figures 2B, 2D, S2A, and S2B). As in the first cohort, we observed that tip and proliferating ECs were detected in d21 untreated tumors and largely disappeared upon sunitinib treatment (Figures S2C–S2E). Largely similar EC subtypes were identified in both experimental cohorts, although not every EC subtype was detected in the second cohort because it contained fewer EC numbers (Figures S2F–S2H).

To explore whether TECs co-opted by cancer cells expressed a different gene signature than did ECs from healthy lungs, we compared the transcriptomes of ECs from untreated and sunitinib-treated tumors to publicly available signatures of healthy lung EC phenotypes (Kalucka et al., 2020) by gene set variation analysis (GSVA). Unexpectedly, however, the transcriptome signatures of ECs from arteries, veins, and capillaries in tumors growing via vessel co-option highly resembled those of ECs from healthy tissues (Figure S2I), suggesting that these co-opted TEC phenotypes transcriptionally resembled NECs. In contrast, the transcriptomes of angiogenic (tip, proliferating, and immature) ECs (detected in d21 untreated tumors but not in healthy, quiescent tissues) were distinct from those of the healthy lung EC phenotypes (Figure S2I).

Figure 2. scRNA-seq of cells from a renal cancer experimental lung metastasis model
(A) Scheme of study design of non-EC-enriched cohort (all cell types in the tumor).
(B) t-SNE plot color-coded for metastatic-cell phenotypes.
(C) t-SNE plot color-coded for cells from indicated treatment conditions.
(D) Gene expression levels of top-10 marker genes of metastatic-cell phenotypes.
(E) Scheme of 4T1 model.
(F) Quantification of vascular type in 4T1 model in indicated conditions.
(G) Representative micrographs of H&E staining of lung metastases in 4T1 model. Note how cancer cells invade the surrounding tissue in an irregular/infiltrative manner. Yellow dashed line, border between metastatic and normal area; TN, tumor nodule; HT, healthy tissue.
(H) Representative micrograph of vessel co-option 4T1 breast cancer lung metastasis section, immunostained for PDPN (pneumocytes) and Hoechst (nuclei). Image on the right is a magnification of the boxed area. Note how the metastasis invades the surrounding lung tissue in an irregular/infiltrative manner with preservation of the epithelial structure.
(I) Quantification of the percentage of proliferating ECs in the 4T1 model.
(J) Quantification of ESM-1⁺ ECs per CD34⁺ area in the 4T1 model.
Data are means ± SEM; n = 3–5 (F); n = 4 (I); n = 3 (J); n.s., p > 0.05 by two-tailed unpaired t test (F, I, and J). Scale bar, 150 μm (G); 50 μm (H).
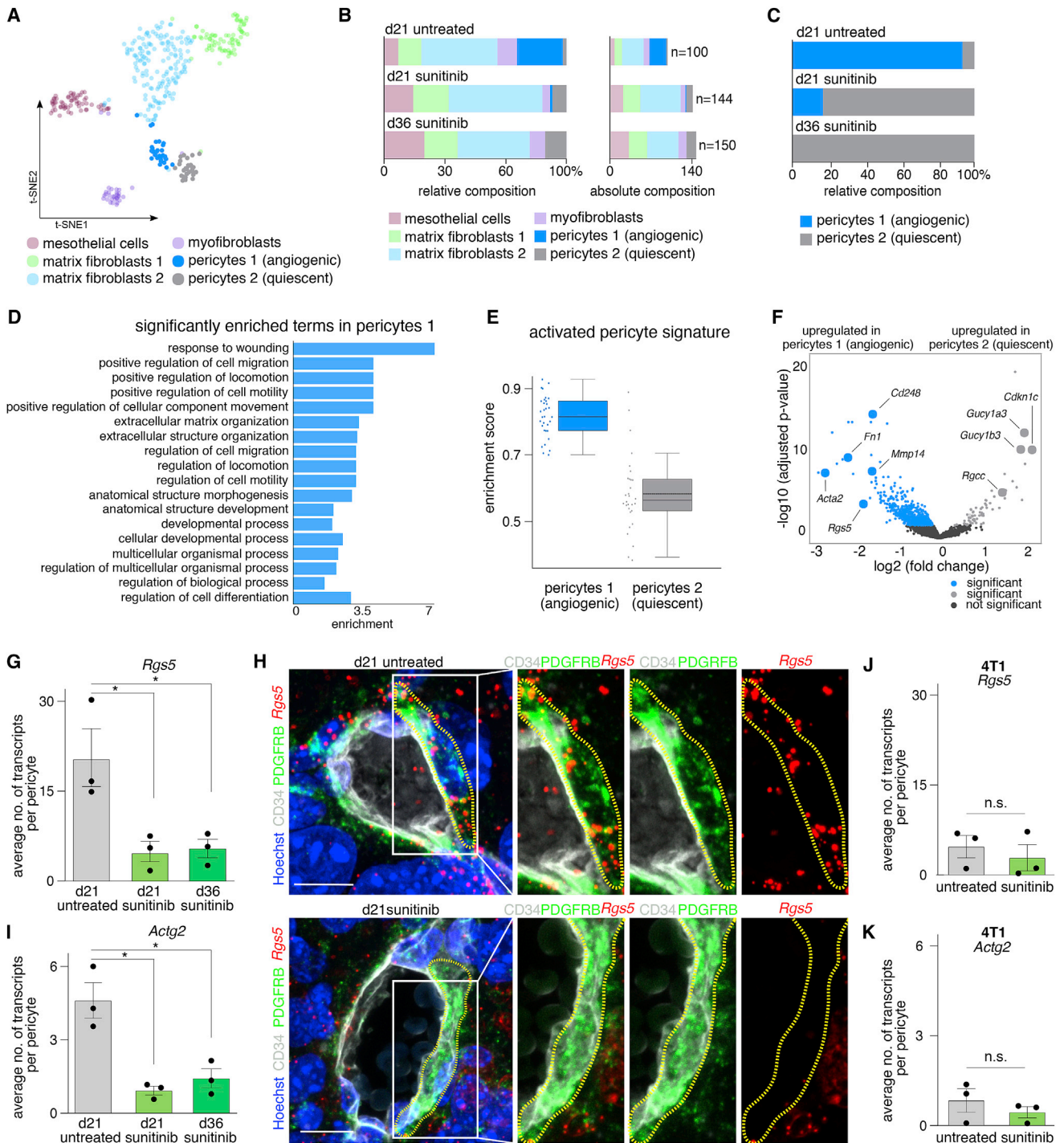See Figure S2 and Tables S1, S2, and S3.

Figure 3. Single-cell analysis of pericytes from vessel co-option metastases

(A) t-SNE plot color-coded for mesenchymal cell subtypes.

(B) Left, relative composition of mesenchymal cell subtypes in indicated conditions, weighted by number of cells per condition. Right, absolute composition of mesenchymal cell subtypes in the indicated conditions.

(C) Relative composition of angiogenic and quiescent pericytes in the indicated conditions, weighted by the number of cells per condition.

(D) Bar graph representation of significantly enriched gene ontology terms (p < 0.001).

(E) Gene set variation analysis with curated angiogenic pericyte gene set. Box height represents interquartile range (IQR); dotted line mean, normal line median; and whiskers, lowest and highest value within respective 1.5 IQR.

(F) Volcano plot of differentially expressed genes in angiogenic versus quiescent pericytes.

(legend continued on next page)

To confirm that angiogenic tip and proliferating TECs are negligibly present during vessel co-option in a metastasis model that grows spontaneously (without sunitinib treatment) via vessel co-option (Bridgeman et al., 2017), we injected 4T1 breast cancer cells into the tail vein of syngeneic BALB/c mice to generate lung metastases characterized by vessel co-option, typified by cancer cells that infiltrated the surrounding tissue in an irregular/infiltrative manner (Figures 2E–2H). Notably, also after sunitinib treatment, these tumors grew by relying on vessel co-option (Figures 2E–2G). Using that model, we confirmed by EdU staining (proliferation) and immunostaining for the tip cell marker ESM-1 a low number of angiogenic ECs (Figures 2I and 2J). Thus, the near absence of tip and proliferating ECs in this model of spontaneous (e.g., not induced by sunitinib) tumor-vessel co-option illustrates that the low numbers of angiogenic TECs are not the result of suppression of these TEC phenotypes by sunitinib but, rather, represent genuine characteristics of tumor-vessel co-option. Although earlier studies suggested that there were fewer proliferating TECs in co-opted tumor vessels (Colpaert et al., 2003; di Tomaso et al., 2011; Lazaris et al., 2018; Sardari Nia et al., 2007; Vermeulen et al., 2001), the near absence of tip TECs was not documented previously. Overall, TECs from sunitinib-treated lung tumors, growing primarily via vessel co-option, seem to exhibit transcriptomic similarities with ECs from healthy lung.

Co-opted pericytes

Using the repeat cohort, in which we sequenced all lung-cell types, we next analyzed co-opted pericytes to explore whether perivascular cells in close contact with co-opting cancer cells might be involved in vessel co-option. We selected 394 mesenchymal cells (Mgp^+) (Bjørklund et al., 2020; Xie et al., 2018), subclustered those cells, and annotated each subcluster by assigning an identity with putative biological features (Figures 3A, S3A, and S3B; Tables S1, S2, and S3). Interestingly, within the pericyte cluster (expressing $Pdgfrb$ [CD140b] and $Mcam$ [CD146] [Armulik et al., 2011; Ferland-McCollough et al., 2017; Yamazaki and Mukouyama, 2018]), we identified two populations (Figures 3A and S3A): (1) one population (pericytes 1) was highly enriched in (almost restricted to) untreated metastases, which grow primarily via vessel sprouting; and (2) a second population (pericytes 2) was nearly absent in angiogenic metastases and, instead, mostly present in sunitinib-treated metastases, growing primarily via vessel co-option (Figures 3B and 3C; Table S4).

To characterize their distinct transcriptome signature, we used a three-step approach. First, we performed a differential gene-expression analysis (Table S5) and selected the top-100 differentially expressed genes for gene ontology (GO) enrichment analysis. In the pericyte population from the untreated (mostly angiogenic) metastases, we detected an expression signature of genes, involved in processes of cellular migration, motility, and extracellular matrix organization (Figure 3D; Table S5). Second, we used GSVA, with a manually curated gene set for activated pericytes involved in vessel sprouting (from the published literature) (Table S5), to score its enrichment in the two pericyte populations. This analysis showed an enrichment of the angiogenic/activated pericyte signature in pericytes from untreated metastases (Figure 3E). Third, when analyzing the top-50 differentially expressed genes in each population, we discovered that pericytes from untreated metastases expressed genes involved in vessel sprouting ($Rgs5$, $Cd248$, and $Fn1$) (Stapor et al., 2014; Teicher, 2019), matrix deposition/remodeling (multiple collagens, $Mmp14$) (Kofler et al., 2015), and motility ($Acta2$ and $Actg2$) (Armulik et al., 2011), whereas pericytes from sunitinib-treated metastases expressed subunits of the nitric oxide receptor-soluble guanylate cyclase, involved in vasodilation ($Gucy1a3$ and $Gucy1b3$) (Chasseigneaux et al., 2018) and genes related to quiescence ($Cdkn1c$ and $Rgcc$) (Figure 3F; Table S5). Altogether, we identified two types of pericytes, one termed an "angiogenic pericyte" phenotype, nearly restricted to the untreated metastases, and another termed "quiescent co-opted pericyte" phenotype, highly enriched in the sunitinib-treated metastases.

We then explored, in two ways, how quiescent, co-opted pericytes were transcriptionally related to healthy lung pericytes. First, after clustering and visualizing the 733 mesenchymal cells that were present in our EC-enriched cohort (Figure S1H), we selected pericytes based on $Pdgfrb$ and $Mcam$ expression, performed graph-based clustering, and, based on the top-50 marker genes, identified two populations: one with a signature of angiogenic and one of quiescent pericytes (Figure S3C; Tables S1 and S2), confirming the results of the repeat cohort. To track the sample origin of each pericyte within these two clusters, we color-coded the clusters for the sample origin, which revealed that quiescent, co-opted pericytes from sunitinib-treated samples clustered together with pericytes from healthy lung (Figures S3C and S3D). Angiogenic pericytes were enriched (93%) in d21 untreated metastases, whereas quiescent, co-opted pericytes were enriched in healthy lung (96%) and in sunitinib-treated samples (100%) (especially after long-term sunitinib treatment) (Figure S3E; Table S4). Jaccard similarity analysis, correlation heatmap with hierarchical clustering and bootstrap analysis, and differential expression analysis of angiogenic versus healthy pericytes (visualized by heatmap) confirmed a high level of similarity between quiescent, co-opted and healthy

---

(G) $Rgs5$ mRNA transcripts per pericyte in metastatic tissue sections in indicated conditions; RNAscope see (H).

(H) Representative RNAscope images of metastatic tissue in the indicated conditions probed for $Rgs5$ (red) mRNA and immunostained for PDGFRB (pericytes), CD34 (ECs), and Hoechst (nuclei). Dotted lines denote pericytes; boxed area is magnified on the right. Scale bar, 10 μm.

(I) Number of $Actg2$ mRNA transcripts per pericyte in metastatic tissue sections in indicated conditions (RNAscope).

(J) Number of $Rgs5$ mRNA transcripts per pericyte in metastatic tissue sections of the 4T1 model in the indicated conditions (RNAscope). n.s., $p > 0.05$ by two-tailed unpaired t test.

(K) Number of $Actg2$ mRNA transcripts per pericyte in metastatic tissue sections of the 4T1 model in the indicated conditions (RNAscope).

Data are means ± SEM; n = 3 (G and I–K); n.s., $p > 0.05$ by two-tailed unpaired t test (J and K); *$p < 0.05$ by one-way ANOVA, with Tukey's multiple comparisons test (G and I).

See Figure S3 and Tables S2, S3, S4, and S5
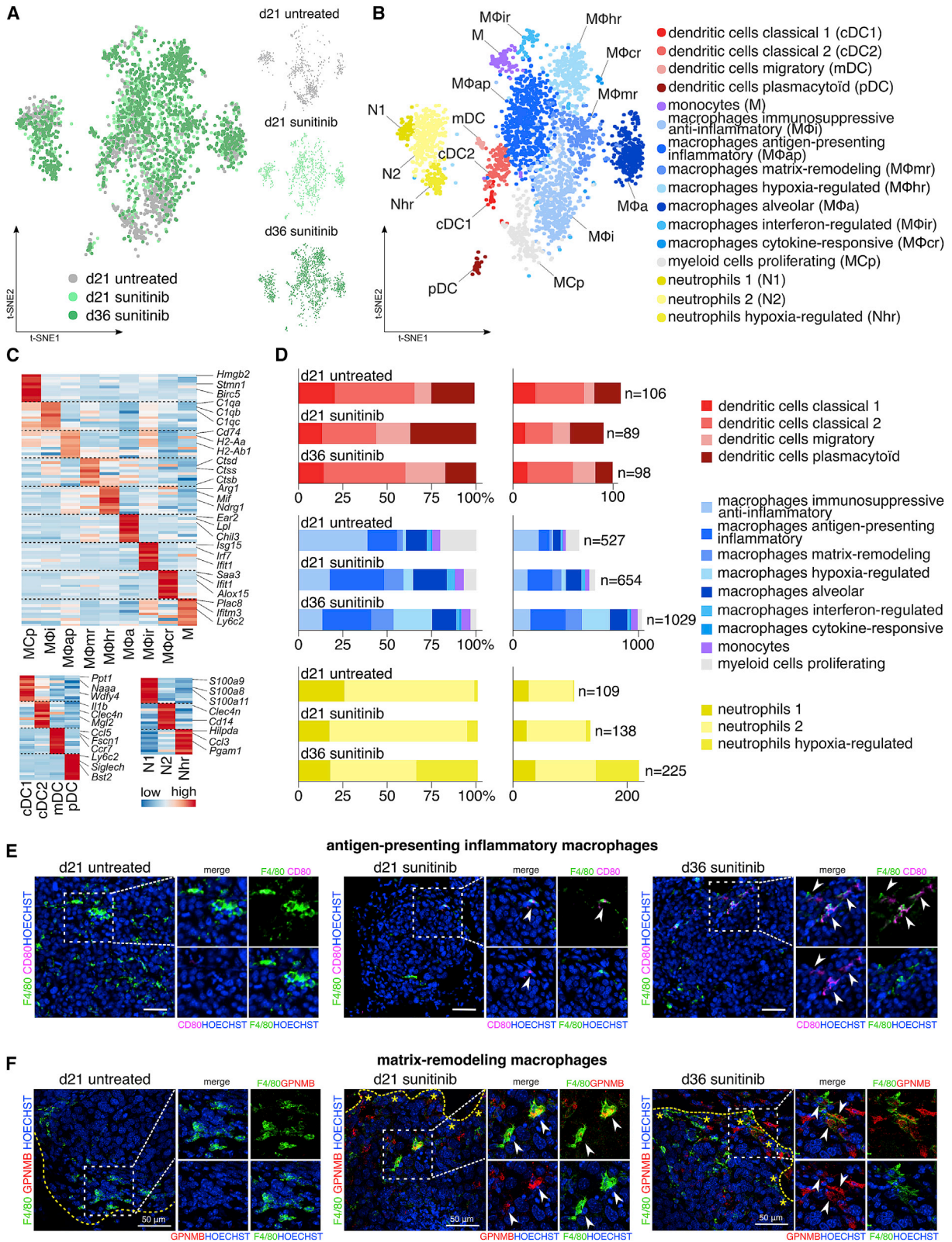
(legend on next page)

pericytes and a clear, distinct transcriptome signature from angiogenic pericytes (Figures S3F–S3H; pericytes in d10 untreated tumors were still quiescent, likely because tumors were small and required more-advanced tumor growth at d21 before adopting an angiogenic phenotype).

Second, we performed an integrated analysis of pericytes from published studies. We used publicly available and previously in-house generated scRNA-seq datasets from murine healthy lung and an untreated angiogenic Lewis lung cancer (LLC) tumor model (Cohen et al., 2018; Goveia et al., 2020; He et al., 2018b; Tabula Muris Consortium et al., 2018; Vanlandewijck et al., 2018) and selected pericytes based on the expression of *Pdgfrb* and *Mcam* (Armulik et al., 2011; Yamazaki and Mukouyama, 2018). We pooled these pericytes with the pericytes from our non-enriched, as well as our EC-enriched, cohorts; applied batch correction (Haghverdi et al., 2018); performed graph-based clustering; and visualized a total of 842 pericytes via t-SNE (Figure S3I; Table S1). This analysis showed that our quiescent, co-opted pericytes clustered together with pericytes from healthy lung, whereas angiogenic pericytes clustered together with pericytes from the angiogenic LLC tumor model (Figures S3J and S3K). GSVA with a gene set containing the top-50 differentially expressed genes of the quiescent, co-opted and angiogenic pericyte population confirmed an enrichment of the quiescent signature in healthy lung pericytes and an enriched angiogenic signature in pericytes from the angiogenic LLC model, as visualized on a t-SNE plot and dotplot (Figures S3L–S3N; Table S5).

To validate our transcriptomics data, we combined immunostaining for pericytes (PDGF-Rß) and ECs (CD34) (Brown et al., 2019) with quantitative RNAscope of the selected angiogenic markers *Rgs5* (known) and *Actg2* (not previously described in tumors). By counting transcript numbers, we confirmed that *Rgs5* and *Actg2* transcript levels were lower in pericytes from co-opted, than angiogenic, metastases (Figures 3G–3I). Together, the transcriptome signature of quiescent co-opted pericytes largely resembled that of healthy lung pericytes.

Using the spontaneous vessel co-option 4T1 metastasis model (Figure 2E), we confirmed by combined immunostaining for pericytes (PDGF-Rß) and ECs (CD34) with RNAscope for angiogenic markers (*Rgs5* and *Actg2*) low transcript levels of angiogenic pericytes (Figures 3J and 3K). Thus, in analogy with TECs, the low number of angiogenic pericytes in co-opted metastases does not only occur upon sunitinib-treatment but also

as an intrinsic characteristic of spontaneously co-opted lung tumor vessels.

Immune cells

Myeloid cells can influence the structure and function of the tumor vasculature and assist cancer-cell invasion and migration (Mazzone and Bergers, 2019); however, a role for myeloid cells in VEGF-blockade-induced vessel co-option has not been explored. We, therefore, characterized the myeloid cell population of 2,975 macrophages, monocytes, dendritic cells, and neutrophils. First, we performed graph-based clustering and annotated a putative biological role for the clusters based on their gene-expression signature (Figures 4A–4D; Tables S1, S2, and S3). We detected a total of 16 myeloid cell subpopulations, putatively identified as four types of dendritic cells (classical 1, classical 2, migratory, and plasmacytoid), three types of neutrophils (neutrophils 1, neutrophils 2, and neutrophils hypoxia-regulated), seven types of macrophages (immunosuppressive/anti-inflammatory, antigen-presenting/inflammatory, matrix-remodeling, hypoxia-regulated, alveolar, interferon-stimulated, and cytokine-responsive), as well as proliferating myeloid cells and monocytes (Figures 4B–4D; Tables S2 and S3).

Antigen-presenting/inflammatory macrophages were characterized by high expression of genes encoding M1-like markers (such as the antigen-presentation machinery), pro-inflammatory markers (such as interleukin [IL]-1β and IL-6) (Hardbower et al., 2017; Pyonteck et al., 2013; Song et al., 2019), as well as interferon gamma (IFNγ) response genes, presumably in response to chronic cell injury because of the sunitinib-induced hypoxia (Figure S4A; Table S2). Immunostaining for a typical marker of M1-like macrophages (CD80 [Bertani et al., 2017], upregulated in this macrophage subtype [Figure S4A]), revealed that antigen-presenting/inflammatory macrophages were especially detected in sunitinib-treated tumors relying on vessel co-option (Figure 4E). GSVA and receptor-ligand interaction analysis-revealed upregulation of genes and gene sets involved in leukocyte-EC interactions in this macrophage subtype (Figures S4B and S4C), as well as an interaction between macrophage-derived transforming growth factor β1 (TGF-β1) and the TGF-β1 receptor on quiescent pericytes (Figure S4C), known to promote pericyte differentiation and adhesion (Armulik et al., 2005; Bergers and Song, 2005; Winkler et al., 2011).

Immunosuppressive/anti-inflammatory macrophages, enriched in untreated angiogenic metastases (Figure 4D; Table

---

Figure 4. Annotation of myeloid cells
(A) t-SNE plot color-coded for myeloid cells from metastatic tissue of the indicated treatment conditions.
(B) t-SNE plot color-coded for myeloid cell subtypes.
(C) Gene expression levels of the top-10 marker genes of myeloid cells subtypes.
(D) Left, relative composition of myeloid cell subtypes in indicated conditions, weighted by the number of cells per condition. Right, absolute composition of myeloid cell subtypes in the indicated conditions.
(E) Representative images of renal cancer lung metastases stained for F4/80 (macrophages), CD80 (M1-like macrophages), and Hoechst (nuclei). Images on the right are magnifications of the respective boxed area of image on the left. Arrowheads, M1-like macrophages.
(F) Representative images of renal cancer lung metastases stained for F4/80 (macrophages), GPNMB (marker of matrix-remodeling macrophages), and Hoechst (nuclei) showing matrix-remodeling macrophages at the invasive front of d36 sunitinib-treated metastases. Images on the right are magnifications of the respective boxed area of the image on the left. GPNMB⁺ F4/80⁻ cells might represent pneumocytes, ECs, or other lung cells (Uhlén et al., 2015). Arrowheads, matrix-remodeling macrophages; asterisks, invasive front; yellow dashed line, border between metastatic and normal area.
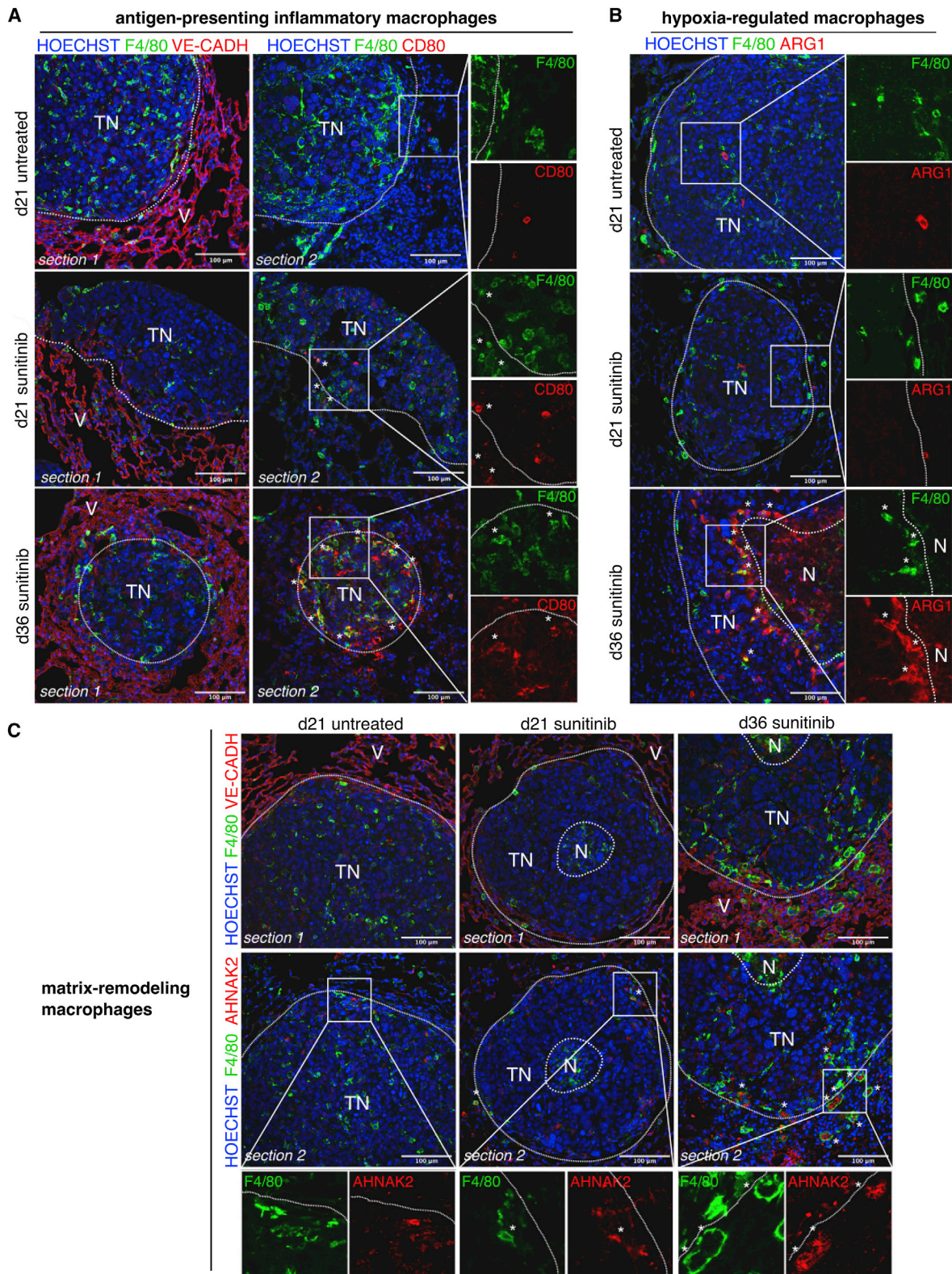Scale bar, 50 μm (E and F).
See Figure S4 and Tables S1, S2, S3, and S4.

Figure 5. Spatial localization of macrophage subtypes in relation to blood vessels

(A–C) Representative images of renal cancer lung metastases, immunostained for F4/80 (macrophage marker) and CD80 (A), arginase 1 (B), and AHNAK2 (C) (markers of antigen-presenting inflammatory, hypoxia-regulated macrophages, and matrix-remodeling macrophages, respectively), as well as for F4/80 and

(legend continued on next page)

S4), were distinguished by expression of canonical (e.g., *Mrc1*, *Lyve1*, and *Cx3cr1*) and non-canonical (e.g., *C1qa*, *C1qb*, *C1qc*, and *Cxcl16*) M2-like markers, which have been related to immunosuppression but also to angiogenesis (Bohlson et al., 2014; Kim et al., 2019) (Figure S4A; Tables S2 and S3). Hypoxia-regulated macrophages, enriched in sunitinib-treated tumors (Figure 4D; Table S4), expressed *Arg1* (marker of M2-like macrophages [Biswas and Mantovani, 2010; van Dalen et al., 2018]) as one of the first top-ranking marker genes (Table S2), as well as other canonical M2-like markers (*Msr1*, *Il1rn*, and *Ccl24* [Azizi et al., 2018; Qian et al., 2020]), likely resulting from the hypoxia (induced by the anti-angiogenic effect of sunitinib) (Figure S1E), known to promote immunosuppressive features (Figure S4A) (Ke et al., 2019). As previously described (Doedens et al., 2010; Takeda et al., 2010), hypoxia-regulated macrophages also increased the expression of inducible nitric oxide synthase (iNOS; *Nos2*; Figure S4A), known to induce T cell suppression directly via nitric oxide production by tumor-associated macrophages (TAMs) and, indirectly, via L-arginine depletion (Doedens et al., 2010).

It is well appreciated that cancer cells become more invasive during vessel co-option (Döme et al., 2007; Frentzas et al., 2016; Griveau et al., 2018; Vasudev and Reynolds, 2014) and that macrophages assist cancer-cell invasion (Bieniasz-Krzywiec et al., 2019; Harney et al., 2015; Nielsen and Schmid, 2017; Wyckoff et al., 2004). Sunitinib treatment also promoted the differentiation of matrix-remodeling macrophages (Figure 4D; Table S4), characterized by high expression of genes involved in extracellular matrix remodeling (*Ctsd*, *Ctss*, *Ctsb*, *Ctsz*, *Ctsa*, *Mmp19*, *Anpep*, and *Gpnmb*) as well as genes known to be expressed in macrophages that support cancer-cell invasion and migration (*Spp1* [encoding osteopontin], *Cd63*, *Pdpn*, and *Anxa1*) (Figure S4A; Tables S2 and S3) (Bieniasz-Krzywiec et al., 2019; Chou et al., 2016; Krishnan et al., 2018; Lan et al., 2019; Moraes et al., 2018; Saiki et al., 1993; Solinas et al., 2010; Szulzewsky et al., 2015; Vizovišek et al., 2019), raising the question as to whether these matrix-remodeling macrophages might assist cancer cells to invade the surrounding healthy lung tissue. Similarly, GSVA with gene sets involved in collagen and matrix components showed enrichment for collagen catabolism, degradation, formation, and binding as well as regulation of the extracellular matrix (ECM) in matrix-remodeling macrophages (Figure S4D; these gene sets were enriched in hypoxia-regulated macrophages as well, in line with their known function to contribute to ECM turnover (Gilkes et al., 2014; Henze and Mazzone, 2016; Rahat et al., 2011)). In addition, consistent with the TGF-β1-dependent, pro-fibrotic role of macrophages in the lung (Murray et al., 2011), receptor-ligand-interaction analyses detected interactions between macrophage-derived TGF-β1 and the TGF-β1 receptor on pericytes (Figure S4C). Immunostaining for one of the top-ranking

markers of matrix-remodeling macrophages (GPNMB [Table S2]), indeed, revealed that these macrophages were located amid cancer cells at the invasive forefront of sunitinib-treated metastases, whereas they were nearly absent in untreated angiogenic metastases (Figure 4F).

To better understand the spatial location of macrophage subtypes, whose gene signatures suggested a possible role in vascular morphogenesis, in relation to the co-opted vessels, we performed immunostaining for the EC marker vascular endothelial (VE)-cadherin and the pan-macrophage marker F4/80, in combination with prototype markers of antigen-presenting/inflammatory (CD80), matrix-remodeling (AHNAK2, a member of the AHNAK family, involved in cell structure, migration, and invasion [Wang et al., 2020; Zhang et al., 2020]), and hypoxia-regulated (arginase 1) macrophages (Figures 5A–5C and S4A). This analysis indeed revealed that antigen-presenting/inflammatory macrophages were positioned in the peripheral rim of the tumor nodules, the tumor region that contains co-opted vessels (Figure 5A). Hypoxia-related macrophages were located in the hypoxic rim surrounding the necrotic core in d36-treated metastases (Figures 5B and S1E). Matrix-remodeling macrophages were located near co-opted vessels at the invasive forefront of metastases (Figure 5C), in line with their increased expression of gene sets involved in leukocyte-EC interactions (Figure S4B). Sunitinib treatment did not seem to affect the subpopulations of the lymphoid lineage (Figures S4E and S4F; Tables S1, S2, S3, and S4). Overall, these transcriptomic results may suggest a putative involvement of macrophage subtypes in tumor-vessel co-option.

Cancer cells

We characterized the cancer-cell population to explore whether cancer-cell subpopulations expressed different transcriptome signatures in tumors growing primarily via vessel co-option. We subclustered 2,613 cancer cells and identified seven populations; of which, two contained actively cycling cancer cells (Figures S5A–S5C; Tables S1, S2, and S4). To mitigate the confounding effect of the cell cycle on the analysis of the non-cycling cancer cells (Luecken and Theis, 2019), we subclustered the non-cycling cancer cells independently (Figures 6A and 6B; Table S1). This analysis showed that cancer cells from untreated and sunitinib-treated metastases largely grouped separately (Figure 6A) and clustered in five different populations (Figures 6B and 6C). We annotated a putative biological role for those clusters by analyzing their gene-expression signatures (Tables S2 and S3). We detected (1) "generic" cancer cells (so-called because they only expressed markers detected in all other cancer-cell clusters, without expressing a distinctive transcriptome signature); (2) stressed cancer cells (as previously identified and characterized [Puram et al., 2017]), likely because sunitinib blocks multiple molecular targets

---

VE-cadherin (EC marker), on consecutive slides for (A) and (C); in (B), F4/80/VE-cadherin staining is not shown because of the peri-necrotic location of the hypoxia-regulated macrophages. Note the localization of CD80+ macrophages, white asterisk in (A), in the peripheral rim of the tumor noduli (where vessels become co-opted), and the proximity to the necrotic regions of hypoxia-regulated macrophages, white asterisk in (B). Matrix-remodeling AHNAK2+ macrophages, white asterisk in (C), lie at the invasive forefront of the tumor nodules. The tumor nodules contain blood vessels with lower VE-cadherin expression. Nuclei are counterstained with Hoechst. Images to the right and below are magnifications of the respective boxed areas of images on the left and above. F4/80−, CD80+ cells might represent T or B cells; scale bar, 100 μm; V, vessels; TN, tumor nodule; N, necrotic center.
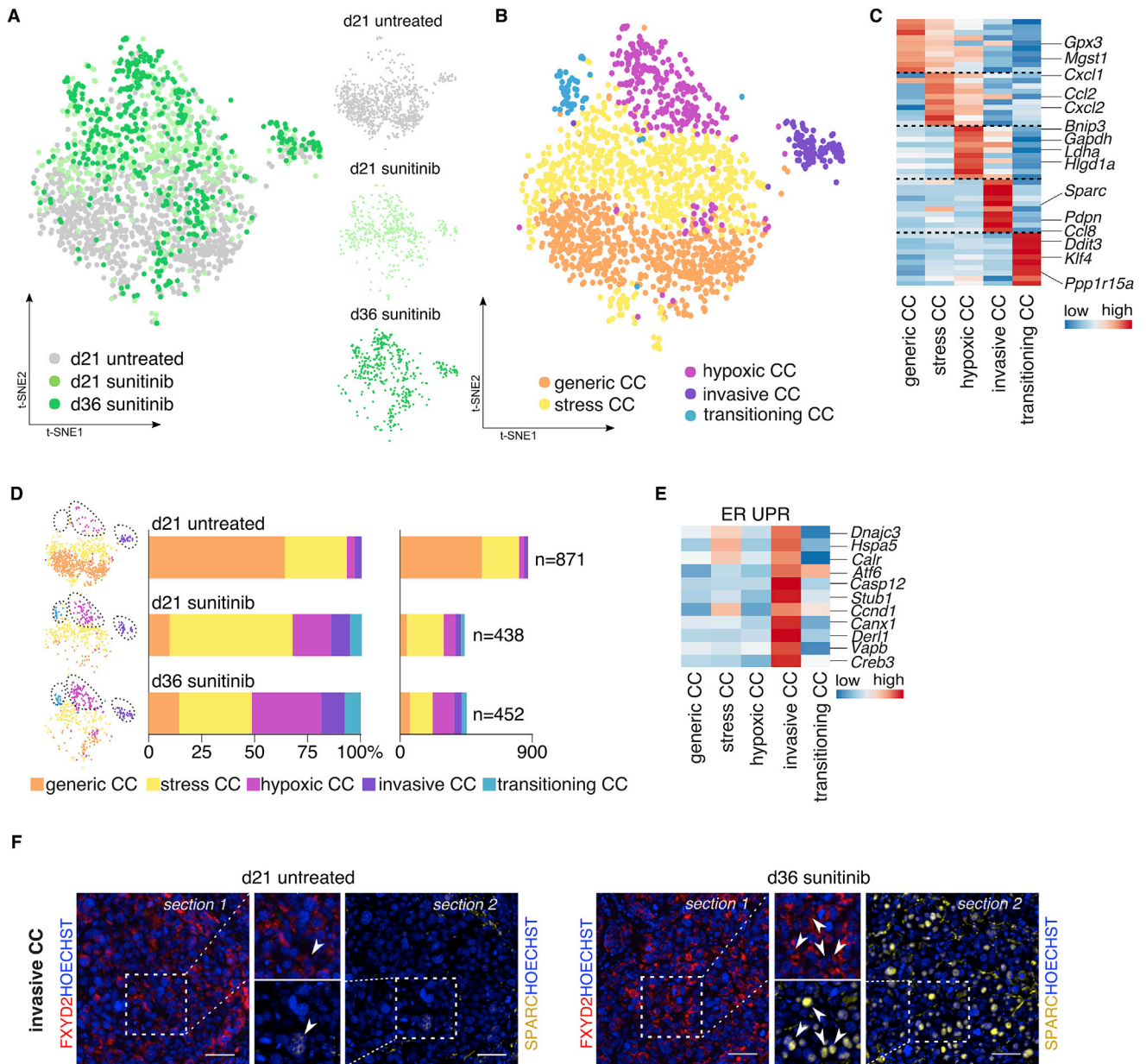
Figure 6. Non-cycling cancer cell subtypes and clinical correlation

(A) t-SNE plot, color-coded for non-cycling cancer cells from metastatic tissue of the indicated treatment conditions.

(B) t-SNE plot color-coded for non-cycling cancer-cell subtypes.

(C) Gene expression levels of top-10 marker genes of non-cycling cancer-cell subtypes.

(D) Left, relative composition of non-cycling cancer-cell subtypes in the indicated conditions, weighted by the number of cells per condition. Right, absolute composition of non-cycling cancer-cell subtypes in the indicated conditions.

(E) Expression levels of genes involved in the endoplasmic reticulum (ER) and unfolded protein response (UPR).

(F) Representative images of renal cancer lung metastases, stained for FXYD2 (marker of cancer cells) and SPARC (marker of invasive cancer cells) on adjacent sections. Nuclei are counterstained with Hoechst. Images in the middle are magnifications of the respective boxed area. Arrowheads, invasive cancer cells; scale bar, 50 μm.

See Figure S5 and Tables S1, S2, S3, and S4.

(Figures 6B–6D); (3) hypoxic cancer cells (Figures 6B–6D, S5D, and S5E), likely because of the hypoxia caused by the anti-angiogenic activity of sunitinib (Figure S1E) (Faivre et al., 2007); and (4) transitioning cancer cells (with increased RNA translation machinery), possibly transitioning to and adopting another phenotype (Figures 6B–6D).

Previous work has proven the importance of cancer-cell migration and invasion during vessel co-option (Döme et al., 2007; Frentzas et al., 2016; Griveau et al., 2018; Vasudev and Reynolds, 2014). In agreement, in our model, we also detected a fraction of invasive cancer cells in sunitinib-treated tumors. These cells (typified by *Serping1* and *Sparc* expression [Chen et al., 2012; Guweidhi et al., 2005; Valiente et al., 2014]) expressed genes involved in the epithelial-to-mesenchymal transition (EMT) (*Spp1*, *Lcn2*, and *Aebp1*) (Kothari et al., 2016; Liu et al., 2018; Madden et al., 2019; Rodvold et al., 2012), endoplasmic reticulum stress, and the unfolded protein response (*Dnajc3*, *Hspa5*, and *Calr*) (Petrova et al., 2008; Wang et al., 2017; Xu et al., 2005), known to promote EMT (Madden et al., 2019) (Figure 6E; Table S2). Immunostaining for SPARC (one of the top markers of invasive cancer cells [Table S2]) and FXYD2 (one of the top general markers of the cancer-cell population) on consecutive slides revealed that invasive cancer cells were enriched in long-term sunitinib-treated vessel-co-option metastases (Figure 6F).

DISCUSSION

We conducted this tumor-vessel co-option single-cell analysis to identify cellular phenotypes exhibiting transcriptome signature changes that might suggest a possible contribution to vessel co-option and obtained the following insights.

Co-opted endothelial cell phenotypes

We observed that co-opted vessels are nearly devoid of angiogenic tip and proliferating ECs, both in an AAT-induced and spontaneous model of tumor-vessel co-option, thereby extending earlier staining reports of a lower proliferation rate of co-opted ECs than that of angiogenic ECs in human tumors (Colpaert et al., 2003; di Tomaso et al., 2011; Lazaris et al., 2018; Sardari Nia et al., 2007; Vermeulen et al., 2001).

A clinically relevant question is whether co-opted ECs up-regulate the expression of specific and potentially targetable markers. Earlier studies documented maintained or altered expression of EC markers (GLUT-1, PGP, CD71 [Bernsen et al., 2005; di Tomaso et al., 2011; Leenders et al., 2004], LYVE-1, CD34 [Stessels et al., 2004; Vermeulen et al., 2001], and CD276 [Seaman et al., 2017]) in co-opted tumor vessels, although several of these markers are also upregulated in other types of tumor vascularization (Kraan et al., 2014; Moore et al., 2018; Qian et al., 2020). Using an unbiased approach, we observed that co-opted ECs in tumor vessels exhibit many transcriptomic similarities with quiescent ECs in healthy vessels. This was unexpected, given that cancer cells can activate ECs in co-culture *in vitro* and in the tumor setting *in vivo* (Folkman and Haudenschild, 1980; Khodarev et al., 2003; Lopes-Bastos et al., 2016). Even though it could be argued that sunitinib treatment rendered TECs quiescent and prevented angiogenic activation, co-opted TECs in the untreated 4T1 tumor model with spontaneous vessel co-option (without sunitinib treatment) were also quiescent.

Co-opted pericyte phenotypes

Like co-opted TECs, co-opted tumor pericytes expressed a gene signature of quiescence, in contrast to pericytes in tumors growing via vessel sprouting, which expressed a gene signature of cellular activation and migration. For vessels to grow, pericytes need to detach so that sprouting ECs can form new vessels. The activation signature of pericytes during vessel sprouting is, thus, to be expected, but the quiescence signature of pericytes during vessel cooption is surprising, given that cancer cells can activate pericytes (Abramsson et al., 2003; Andrae et al., 2008; Furuhashi et al., 2004). This raises the question of whether, and/or to what extent, pericyte quiescence is a cause or a consequence of vessel co-option. It is well established that pericytes, when covering nascent EC channels, render ECs quiescent and help to mature the newly formed vessel, whereas quiescent ECs, in turn, can promote pericyte coverage (Benjamin et al., 1998; Cantelmo et al., 2016; Carmeliet and Jain, 2011; Hellström et al., 1999, 2001; Herbert and Stainier, 2011). Conversely, activated angiogenic ECs can also induce pericyte activation and migration (Gaengel et al., 2009; Potente et al., 2011; Ribatti et al., 2011). Pericytes were also quiescent in the 4T1 tumor model, in which vessel co-option occurs spontaneously.

Only a few markers of angiogenic pericytes (*Rgs5*, *Cd248*, *Cspg4*, and *Acta2*) (Armulik et al., 2011; Bondjers et al., 2003; Simonavicius et al., 2008; Teicher, 2019) have been reported to date. An integrated, unbiased analysis of pericytes from our, and other publicly available, datasets identified previously unrecognized markers (*Col18a1*, *Actg2*, and *Serpina1b*), which might facilitate future identification of angiogenic pericytes in other studies.

Blockade of platelet-derived growth factor receptor beta (PDGFRβ) signaling by sunitinib or other agents promotes the detachment and depletion of tumor-associated pericytes (Abramsson et al., 2003; Bergers et al., 2003; Shaheen et al., 2001; Song et al., 2005; Yokoi et al., 2005), precisely the opposite of what we observed. Because pericytes are quiescent in co-opted vessels, it is unlikely that PDGFRβ inhibition by sunitinib was responsible for the co-opted pericyte phenotype. This raises the question of whether co-opting cancer cells or macrophages might signal to pericytes (and ECs) to render them quiescent. Indeed, support for this hypothesis stems from data in an *in vitro* pericyte-glioblastoma co-culture model (not treated with AAT), in which co-opting cancer cells impaired the contractility of pericytes (Caspani et al., 2014). Moreover, invasive co-opting cancer cells highly expressed *Serpinf1*, encoding the anti-angiogenic and pericyte-protective factor pigment-epithelium-derived factor (PEDF) (Dawson et al., 1999; Doll et al., 2003), whereas quiescent pericytes upregulated its receptor *Pdxcl1* (Figures S5F and S5G), possibly suggesting a quiescence-inducing interaction.

Macrophages could be involved in a similar intercellular crosstalk. Interaction between TGF-β1 derived from macrophages and TGF-β1 receptor on quiescent pericytes can promote pericyte adhesion, differentiation, and coverage of ECs (Armulik et al., 2005; Bergers and Song, 2005; Winkler et al., 2011), suggesting a potential involvement of these macrophages in the quiescent pericyte phenotype in co-opted metastases. In

addition, M1-like polarization of macrophages in murine tumors promotes tumor vessel normalization with increased pericyte coverage (Jarosz-Biej et al., 2018; Rolny et al., 2011; Van de Veire et al., 2010), raising the question whether M1-like macrophages might be involved in maintaining a normal quiescent vascular phenotype, despite vessel co-option, preventing co-opted vessel disorganization and/or promoting normalization of disorganized co-opted vessels. Indeed, M1-like antigen-presenting/inflammatory macrophages did localize in the invasive front of tumor areas, in which vessels are being co-opted in sunitinib-treated metastases, and expressed markers involved in leukocyte-EC interactions. Furthermore, M1-like macrophages express cytokines (IL-12, IFNγ, and TNFα) that promote vessel normalization and quiescence (Gerber et al., 2003; He et al., 2018a; Liu et al., 2011; Lu et al., 2015; Porcellini et al., 2015).

Immune cell phenotypes

A role for immune cells in tumor-vessel co-option has not been considered to date. However, TAMs can affect tumor vascularization, modulate the refractoriness to AAT (Chung et al., 2013; Shojaei et al., 2007, 2009; Tazzyman et al., 2013; Yang et al., 2004), and assist cancer-cell invasion and migration (Condeelis and Pollard, 2006; Nielsen and Schmid, 2017; Wyckoff et al., 2004), a hallmark of vessel co-option (Donnem et al., 2018; Kuczynski et al., 2019). Interestingly, sunitinib-treated metastases, growing primarily via vessel co-option, were enriched in antigen-presenting/inflammatory macrophages, the phenotype of which might be partly due to blockade of the CSF-1 receptor and VEGFR family members (especially VEGFR1) on macrophages by sunitinib, known to promote M1-like macrophage polarization (Pyonteck et al., 2013; Rolny et al., 2011; Zhu et al., 2014). Sunitinib-treated metastases also showed a predominant enrichment in matrix-remodeling macrophages. Based on their expression signature of genes involved in matrix degradation and deposition, we speculate that this macrophage subtype might be able to assist invasive cancer cells to co-opt healthy lung vessels. For co-opting cancer cells to travel alongside pre-existing blood vessels, they must make their way through the interstitial stroma, which is dense in ECM. Matrix-remodeling macrophages might assist co-opting cancer cells by paving the way through matrix reorganization, involving degradation of the existing matrix (facilitating invasion by cancer cells) and deposition of the new matrix (anchor points for invading cancer cells). This hypothesis is further supported by our findings that these macrophages were located at the invasive forefront of co-opting metastases, where blood vessels become co-opted by cancer cells. Further, matrix-remodeling macrophages are known to facilitate cancer-cell extravasation and dissemination (Bieniasz-Krzywiec et al., 2019; Szulzewsky et al., 2015).

Co-opting cancer cell phenotypes

To date, co-opting cancer cells have been largely investigated by immunostaining/morphological analyses (Auf et al., 2010; Griveau et al., 2018; Hu et al., 2005; Kuczynski et al., 2016; Sakariassen et al., 2006). In general, cancer cells from sunitinib-treated mice (predominantly co-opting cancer cells) exhibited a greater phenotypic heterogeneity than did cancer cells from untreated mice (mainly angiogenic cancer cells). In line with earlier studies documenting an increased motility and invasiveness of co-opting cancer cells (Döme et al., 2007; Frentzas et al., 2016; Griveau et al., 2018; Kuczynski et al., 2016; Vasudev and Reynolds, 2014), we identified an invasive cancer-cell subtype that is enriched in metastases growing via vessel co-option. Whether the invasiveness of this cancer-cell subpopulation is fueled by hypoxia (caused by vessel regression from sunitinib treatment), as has been documented previously (Ebos et al., 2009; Pàez-Ribes et al., 2009), remains to be studied. Of note, when assessing the expression of previously studied markers of co-opting cancer cells, we observed that invasive cancer cells highly expressed *Wnt7b* (Figure S5H), documented to promote cancer-cell invasion and vessel co-option in a glioma model (Griveau et al., 2018).

Tumors relying on vessel sprouting often outgrow their vascular supply, causing central hypoxia. Additional AAT aggravates intra-tumoral hypoxia. Although hypoxia is a strong stimulus of vessel sprouting (Pugh and Ratcliffe, 2003; Rey et al., 2017), AAT by sunitinib inhibits this rescue process, forcing cancer cells to seek an alternative tumor-vascularization mechanism. Hence, they become invasive to co-opt pre-existing tissue vessels, taking advantage of the normal oxygenation of healthy tissues.

Possible translational implications

Our study raises questions on how to design clinical strategies to overcome tumor-vessel co-option as a resistance mechanism against VEGF-targeted AAT or even for tumors that rely spontaneously on vessel co-option. First, the finding that co-opted ECs were transcriptionally largely similar to their healthy counterparts raises concerns about whether a strategy targeting co-opted TECs can be a safe treatment option for vessel co-option because such treatment strategy will unavoidably also affect healthy NECs across the body. A similar argument applies to the vascular pericytes. Second, these findings raise the question about whether therapeutic anti-tumor vessel co-option strategies should be targeted to non-vascular cell types, such as promoting M1-like macrophage polarization and/or suppressing the matrix-remodeling macrophages and the invasive cancer-cell phenotypes. In addition, given that AAT aims at targeting angiogenic ECs, the near absence of angiogenic tip and proliferating TECs may provide an explanation for the lack of effectiveness of AAT in patients with tumors growing via vessel co-option (de Groot et al., 2010; Frentzas et al., 2016).

Another translational option might be to take advantage of the altered macrophage features in tumors relying on vessel co-option after AAT. Some of these macrophage populations highly expressed genes, encoding immune checkpoint molecules. For instance, hypoxia-related macrophages expressed PD-L1 (*Cd274*), in line with their reported T cell suppressive function (Doedens et al., 2010; Noman et al., 2014; Wen et al., 2020), whereas antigen-presenting inflammatory macrophages expressed PD-L2 (*Pdcd1lg2*), in line with the late-interferon response of those macrophages (Garcia-Diaz et al., 2017) (Figure S4A). These findings raise the question if immune checkpoint-inhibitor treatment might evoke an improved immune response against the co-opting cancer cells and whether that treatment might synergize with AAT, considering the increasing

evidence of successful combination therapies of AAT and PD-(L) 1 inhibition (Allen et al., 2017; Lee et al., 2020; Schmittnaegel et al., 2017; Wallin et al., 2016).

Limitations of the study

First, we acknowledge that the inferred biological phenotypes are putative, based on bioinformatics analysis combined with literature surveys, and require validation at the protein level. Second, our study is limited by the use of only two mouse models. scRNA-seq analysis of additional spontaneous tumor-vessel co-option models and clinical tumor samples relying on vessel co-option will increase the effect of this study. Third, the role of the identified macrophages and cancer cells in tumor-vessel co-option requires further functional validation.

STAR★METHODS

Detailed methods are provided in the online version of this paper and include the following:

- KEY RESOURCES TABLE
- RESOURCE AVAILABILITY
  - Lead contact
  - Materials availability
  - Data and code availability
- EXPERIMENTAL MODEL AND SUBJECT DETAILS
  - Animals
  - Cell Lines
- METHOD DETAILS
  - Mouse model of renal cancer experimental lung metastasis
  - Mouse model of breast cancer experimental lung metastasis
  - Sunitinib treatment
  - Metastatic cell isolation & tumor and normal endothelial cell isolation
  - Histology, immunohistochemistry and morphometric analysis
  - RNAscope *in situ* hybridization and quantification
  - Bioluminescence imaging
  - Single-cell droplet-based RNA sequencing
  - Single-cell transcriptomics analysis
  - Quality control and data normalization
  - EC-enriched dataset: *in silico* endothelial cell and pericyte selection
  - EC-enriched dataset: batch effect correction
  - EC-enriched dataset: feature selection and dimensionality reduction
  - Non-EC enriched dataset: feature selection and dimensionality reduction
  - Cluster identification
  - Marker gene analysis
  - Cluster annotation
  - Data visualization
  - Gene ontology analysis
  - Gene set enrichment analysis
  - Gene set variation analysis
  - Jaccard similarity analysis

- Meta-analysis of pericytes from published transcriptomics data
- Ligand-receptor interaction analysis
- QUANTIFICATION AND STATISTICAL ANALYSIS
  - Statistical analyses
  - Software

REFERENCES

Abraham, G., Qiu, Y., and Inouye, M. (2017). FlashPCA2: principal component analysis of Biobank-scale genotype datasets. Bioinformatics 33, 2776–2778.

Abramsson, A., Lindblom, P., and Betsholtz, C. (2003). Endothelial and nonendothelial sources of PDGF-B regulate pericyte recruitment and influence vascular pattern formation in tumors. J. Clin. Invest. 112, 1142–1151.

Allen, E., Jabouille, A., Rivera, L.B., Lodewijckx, I., Missiaen, R., Steri, V., Feyen, K., Tawney, J., Hanahan, D., Michael, I.P., and Bergers, G. (2017). Combined antiangiogenic and anti-PD-L1 therapy stimulates tumor immunity through HEV formation. Sci. Transl. Med. 9, eaak9679.

Andrae, J., Gallini, R., and Betsholtz, C. (2008). Role of platelet-derived growth factors in physiology and medicine. Genes Dev. 22, 1276–1312.

Armulik, A., Abramsson, A., and Betsholtz, C. (2005). Endothelial/pericyte interactions. Circ. Res. 97, 512–523.

Armulik, A., Genové, G., and Betsholtz, C. (2011). Pericytes: developmental, physiological, and pathological perspectives, problems, and promises. Dev. Cell 21, 193–215.

Auf, G., Jabouille, A., Guérit, S., Pineau, R., Delugin, M., Bouchecareilh, M., Magnin, N., Favereaux, A., Maitre, M., Gaiser, T., et al. (2010). Inositol-requiring enzyme 1alpha is a key regulator of angiogenesis and invasion in malignant glioma. Proc. Natl. Acad. Sci. USA 107, 15553–15558.

Azizi, E., Carr, A.J., Plitas, G., Cornish, A.E., Konopacki, C., Prabhakaran, S., Nainys, J., Wu, K., Kiseliovas, V., Setty, M., et al. (2018). Single-cell map of diverse immune phenotypes in the breast tumor microenvironment. Cell 174, 1293–1308.e36.

Benjamin, L.E., Hemo, I., and Keshet, E. (1998). A plasticity window for blood vessel remodelling is defined by pericyte coverage of the preformed endothelial network and is regulated by PDGF-B and VEGF. Development 125, 1591–1598.

Bergers, G., and Song, S. (2005). The role of pericytes in blood-vessel formation and maintenance. Neuro-oncol. 7, 452–464.

Bergers, G., Song, S., Meyer-Morse, N., Bergsland, E., and Hanahan, D. (2003). Benefits of targeting both pericytes and endothelial cells in the tumor vasculature with kinase inhibitors. J. Clin. Invest. 111, 1287–1295.

Bernsen, H., Van der Laak, J., Küsters, B., Van der Ven, A., and Wesseling, P. (2005). Gliomatosis cerebri: quantitative proof of vessel recruitment by cooptation instead of angiogenesis. J. Neurosurg. 103, 702–706.

Bertani, F.R., Mozetic, P., Fioramonti, M., Iuliani, M., Ribelli, G., Pantano, F., Santini, D., Tonini, G., Trombetta, M., Businaro, L., et al. (2017). Classification of M1/M2-polarized human macrophages by label-free hyperspectral reflectance confocal microscopy and multivariate analysis. Sci. Rep. 7, 8965.

Bieniasz-Krzywiec, P., Martín-Pérez, R., Ehling, M., García-Caballero, M., Pinioti, S., Pretto, S., Kroes, R., Aldeni, C., Di Matteo, M., Prenen, H., et al. (2019). Podoplanin-Expressing Macrophages Promote Lymphangiogenesis and Lymphoinvasion in Breast Cancer. Cell Metab. 30, 917–936.e10.

Biswas, S.K., and Mantovani, A. (2010). Macrophage plasticity and interaction with lymphocyte subsets: cancer as a paradigm. Nat. Immunol. 11, 889–896.

Bjørklund, G., Svanberg, E., Dadar, M., Card, D.J., Chirumbolo, S., Harrington, D.J., and Aaseth, J. (2020). The role of matrix Gla protein (MGP) in vascular calcification. Curr. Med. Chem. 27, 1647–1660.

Bohlson, S.S., O'Conner, S.D., Hulsebus, H.J., Ho, M.M., and Fraser, D.A. (2014). Complement, c1q, and c1q-related molecules regulate macrophage polarization. Front. Immunol. 5, 402.

Bondjers, C., Kalén, M., Hellström, M., Scheidl, S.J., Abramsson, A., Renner, O., Lindahl, P., Cho, H., Kehrl, J., and Betsholtz, C. (2003). Transcription profiling of platelet-derived growth factor-B-deficient mouse embryos identifies RGS5 as a novel marker for pericytes and vascular smooth muscle cells. Am. J. Pathol. 162, 721–729.

Bridgeman, V.L., Vermeulen, P.B., Foo, S., Bilecz, A., Daley, F., Kostaras, E., Nathan, M.R., Wan, E., Frentzas, S., Schweiger, T., et al. (2017). Vessel co-option is common in human lung metastases and mediates resistance to anti-angiogenic therapy in preclinical lung metastasis models. J. Pathol. 241, 362–374.

Brown, L.S., Foster, C.G., Courtney, J.M., King, N.E., Howells, D.W., and Sutherland, B.A. (2019). Pericytes and neurovascular function in the healthy and diseased brain. Front. Cell. Neurosci. 13, 282.

Cantelmo, A.R., Conradi, L.C., Brajic, A., Goveia, J., Kalucka, J., Pircher, A., Chaturvedi, P., Hol, J., Thienpont, B., Teuwen, L.A., et al. (2016). Inhibition of the glycolytic activator PFKFB3 in endothelium induces tumor vessel normalization, impairs metastasis, and improves chemotherapy. Cancer Cell 30, 968–985.

Carmeliet, P., and Jain, R.K. (2011). Molecular mechanisms and clinical applications of angiogenesis. Nature 473, 298–307.

Caspani, E.M., Crossley, P.H., Redondo-Garcia, C., and Martinez, S. (2014). Glioblastoma: a pathogenic crosstalk between tumor cells and pericytes. PLoS ONE 9, e101402.

Chasseigneaux, S., Moraca, Y., Cochois-Guégan, V., Boulay, A.C., Gilbert, A., Le Crom, S., Blugeon, C., Firmo, C., Cisternino, S., Laplanche, J.L., et al. (2018). Isolation and differential transcriptome of vascular smooth muscle cells and mid-capillary pericytes from the rat brain. Sci. Rep. 8, 12272.

Chen, J., Wang, M., Xi, B., Xue, J., He, D., Zhang, J., and Zhao, Y. (2012). SPARC is a key regulator of proliferation, apoptosis and invasion in human ovarian cancer. PLoS ONE 7, e42413.

Chou, J., Chan, M.F., and Werb, Z. (2016). Metalloproteinases: a functional pathway for myeloid cells. Microbiol. Spectr. 4, 4.2.18.

Chung, A.S., Wu, X., Zhuang, G., Ngu, H., Kasman, I., Zhang, J., Vernes, J.M., Jiang, Z., Meng, Y.G., Peale, F.V., et al. (2013). An interleukin-17-mediated paracrine network promotes tumor resistance to anti-angiogenic therapy. Nat. Med. 19, 1114–1123.

Cohen, M., Giladi, A., Gorki, A.D., Solodkin, D.G., Zada, M., Hladik, A., Miklosi, A., Salame, T.M., Halpern, K.B., David, E., et al. (2018). Lung single-cell signaling interaction map reveals basophil role in macrophage imprinting. Cell 175, 1031–1044.e18.

Colpaert, C.G., Vermeulen, P.B., Van Beest, P., Soubry, A., Goovaerts, G., Dirix, L.Y., Harris, A.L., and Van Marck, E.A. (2003). Cutaneous breast cancer deposits show distinct growth patterns with different degrees of angiogenesis, hypoxia and fibrin deposition. Histopathology 42, 530–540.

Condeelis, J., and Pollard, J.W. (2006). Macrophages: obligate partners for tumor cell migration, invasion, and metastasis. Cell 124, 263–266.

Dawson, D.W., Volpert, O.V., Gillis, P., Crawford, S.E., Xu, H., Benedict, W., and Bouck, N.P. (1999). Pigment epithelium-derived factor: a potent inhibitor of angiogenesis. Science 285, 245–248.

de Groot, J.F., Fuller, G., Kumar, A.J., Piao, Y., Eterovic, K., Ji, Y., and Conrad, C.A. (2010). Tumor invasion after treatment of glioblastoma with bevacizumab: radiographic and pathologic correlation in humans and mice. Neuro-oncol. 12, 233–242.

di Tomaso, E., Snuderl, M., Kamoun, W.S., Duda, D.G., Auluck, P.K., Fazlollahi, L., Andronesi, O.C., Frosch, M.P., Wen, P.Y., Plotkin, S.R., et al. (2011). Glioblastoma recurrence after cediranib therapy in patients: lack of "rebound" revascularization as mode of escape. Cancer Res. 71, 19–28.

Doedens, A.L., Stockmann, C., Rubinstein, M.P., Liao, D., Zhang, N., DeNardo, D.G., Coussens, L.M., Karin, M., Goldrath, A.W., and Johnson, R.S. (2010). Macrophage expression of hypoxia-inducible factor-1 alpha suppresses T-cell function and promotes tumor progression. Cancer Res. 70, 7465–7475.

Doll, J.A., Stellmach, V.M., Bouck, N.P., Bergh, A.R., Lee, C., Abramson, L.P., Cornwell, M.L., Pins, M.R., Borensztajn, J., and Crawford, S.E. (2003). Pigment epithelium-derived factor regulates the vasculature and mass of the prostate and pancreas. Nat. Med. 9, 774–780.

Döme, B., Hendrix, M.J., Paku, S., Tóvári, J., and Tímár, J. (2007). Alternative vascularization mechanisms in cancer: Pathology and therapeutic implications. Am. J. Pathol. 170, 1–15.

Donnem, T., Reynolds, A.R., Kuczynski, E.A., Gatter, K., Vermeulen, P.B., Kerbel, R.S., Harris, A.L., and Pezzella, F. (2018). Non-angiogenic tumours and their influence on cancer biology. Nat. Rev. Cancer 18, 323–336.

Ebos, J.M., Lee, C.R., Cruz-Munoz, W., Bjarnason, G.A., Christensen, J.G., and Kerbel, R.S. (2009). Accelerated metastasis after short-term treatment with a potent inhibitor of tumor angiogenesis. Cancer Cell 15, 232–239.

Eden, E., Navon, R., Steinfeld, I., Lipson, D., and Yakhini, Z. (2009). GOrilla: a tool for discovery and visualization of enriched GO terms in ranked gene lists. BMC Bioinformatics 10, 48.

Efremova, M., Vento-Tormo, M., Teichmann, S.A., and Vento-Tormo, R. (2020). CellPhoneDB: inferring cell-cell communication from combined expression of multi-subunit ligand-receptor complexes. Nat. Protoc. 15, 1484–1506.

Faivre, S., Demetri, G., Sargent, W., and Raymond, E. (2007). Molecular basis for sunitinib efficacy and future clinical development. Nat. Rev. Drug Discov. 6, 734–745.

Ferland-McCollough, D., Slater, S., Richard, J., Reni, C., and Mangialardi, G. (2017). Pericytes, an overlooked player in vascular pathobiology. Pharmacol. Ther. 171, 30–42.

Folkman, J., and Haudenschild, C. (1980). Angiogenesis in vitro. Nature 288, 551–556.

Frentzas, S., Simoneau, E., Bridgeman, V.L., Vermeulen, P.B., Foo, S., Kostaras, E., Nathan, M., Wotherspoon, A., Gao, Z.H., Shi, Y., et al. (2016). Vessel co-option mediates resistance to anti-angiogenic therapy in liver metastases. Nat. Med. 22, 1294–1302.

Furuhashi, M., Sjöblom, T., Abramsson, A., Ellingsen, J., Micke, P., Li, H., Bergsten-Folestad, E., Eriksson, U., Heuchel, R., Betsholtz, C., et al. (2004). Platelet-derived growth factor production by B16 melanoma cells leads to increased pericyte abundance in tumors and an associated increase in tumor growth rate. Cancer Res. 64, 2725–2733.

Gaengel, K., Genové, G., Armulik, A., and Betsholtz, C. (2009). Endothelial-mural cell signaling in vascular development and angiogenesis. Arterioscler. Thromb. Vasc. Biol. 29, 630–638.

Galili, T., O'Callaghan, A., Sidi, J., and Sievert, C. (2018). heatmaply: an R package for creating interactive cluster heatmaps for online publishing. Bioinformatics 34, 1600–1602.

Garcia-Diaz, A., Shin, D.S., Moreno, B.H., Saco, J., Escuin-Ordinas, H., Rodriguez, G.A., Zaretsky, J.M., Sun, L., Hugo, W., Wang, X., et al. (2017). Interferon receptor signaling pathways regulating PD-L1 and PD-L2 expression. Cell Rep. 19, 1189–1201.

Gerber, S.A., Moran, J.P., Frelinger, J.G., Frelinger, J.A., Fenton, B.M., and Lord, E.M. (2003). Mechanism of IL-12 mediated alterations in tumour blood vessel morphology: analysis using whole-tissue mounts. Br. J. Cancer 88, 1453–1461.

Gilkes, D.M., Semenza, G.L., and Wirtz, D. (2014). Hypoxia and the extracellular matrix: drivers of tumour metastasis. Nat. Rev. Cancer 14, 430–439.

Goveia, J., Rohlenova, K., Taverna, F., Treps, L., Conradi, L.C., Pircher, A., Geldhof, V., de Rooij, L.P.M.H., Kalucka, J., Sokol, L., et al. (2020). An integrated gene expression landscape profiling approach to identify lung tumor endothelial cell heterogeneity and angiogenic candidates. Cancer Cell 37, 21–36.e13.

Griveau, A., Seano, G., Shelton, S.J., Kupp, R., Jahangiri, A., Obernier, K., Krishnan, S., Lindberg, O.R., Yuen, T.J., Tien, A.C., et al. (2018). A glial signature and Wnt7 signaling regulate glioma-vascular interactions and tumor microenvironment. Cancer Cell 33, 874–889.e7.

Guweidhi, A., Kleeff, J., Adwan, H., Giese, N.A., Wente, M.N., Giese, T., Büchler, M.W., Berger, M.R., and Friess, H. (2005). Osteonectin influences growth and invasion of pancreatic cancer cells. Ann. Surg. 242, 224–234.

Haghverdi, L., Lun, A.T.L., Morgan, M.D., and Marioni, J.C. (2018). Batch effects in single-cell RNA-sequencing data are corrected by matching mutual nearest neighbors. Nat. Biotechnol. 36, 421–427.

Hänzelmann, S., Castelo, R., and Guinney, J. (2013). GSVA: gene set variation analysis for microarray and RNA-seq data. BMC Bioinformatics 14, 7.

Hardbower, D.M., Coburn, L.A., Asim, M., Singh, K., Sierra, J.C., Barry, D.P., Gobert, A.P., Piazuelo, M.B., Washington, M.K., and Wilson, K.T. (2017). EGFR-mediated macrophage activation promotes colitis-associated tumorigenesis. Oncogene 36, 3807–3819.

Harney, A.S., Arwert, E.N., Entenberg, D., Wang, Y., Guo, P., Qian, B.Z., Oktay, M.H., Pollard, J.W., Jones, J.G., and Condeelis, J.S. (2015). Real-time imaging reveals local, transient vascular permeability, and tumor cell intravasation stimulated by TIE2hi macrophage-derived VEGFA. Cancer Discov. 5, 932–943.

He, B., Jabouille, A., Steri, V., Johansson-Percival, A., Michael, I.P., Kotamraju, V.R., Junckerstorff, R., Nowak, A.K., Hamzah, J., Lee, G., et al. (2018a). Vascular targeting of LIGHT normalizes blood vessels in primary brain cancer and induces intratumoural high endothelial venules. J. Pathol. 245, 209–221.

He, L., Vanlandewijck, M., Mäe, M.A., Andrae, J., Ando, K., Del Gaudio, F., Nahar, K., Lebouvier, T., Laviña, B., Gouveia, L., et al. (2018b). Single-cell RNA sequencing of mouse brain and lung vascular and vessel-associated cell types. Sci. Data 5, 180160.

Hellström, M., Kalén, M., Lindahl, P., Abramsson, A., and Betsholtz, C. (1999). Role of PDGF-B and PDGFRβ in recruitment of vascular smooth muscle cells and pericytes during embryonic blood vessel formation in the mouse. Development 126, 3047–3055.

Hellström, M., Gerhardt, H., Kalén, M., Li, X., Eriksson, U., Wolburg, H., and Betsholtz, C. (2001). Lack of pericytes leads to endothelial hyperplasia and abnormal vascular morphogenesis. J. Cell Biol. 153, 543–553.

Henze, A.T., and Mazzone, M. (2016). The impact of hypoxia on tumor-associated macrophages. J. Clin. Invest. 126, 3672–3679.

Herbert, S.P., and Stainier, D.Y. (2011). Molecular control of endothelial cell behaviour during blood vessel morphogenesis. Nat. Rev. Mol. Cell Biol. 12, 551–564.

Heskes, T., Eisinga, R., and Breitling, R. (2014). A fast algorithm for determining bounds and accurate approximate p-values of the rank product statistic for replicate experiments. BMC Bioinformatics 15, 367.

Hu, J., Bianchi, F., Ferguson, M., Cesario, A., Margaritora, S., Granone, P., Goldstraw, P., Tetlow, M., Ratcliffe, C., Nicholson, A.G., et al. (2005). Gene expression signature for angiogenic and nonangiogenic non-small-cell lung cancer. Oncogene 24, 1212–1219.

Jarosz-Biej, M., Kamińska, N., Matuszczak, S., Cichoń, T., Pamuła-Piłat, J., Czapla, J., Smolarczyk, R., Skwarzyńska, D., Kulik, K., and Szala, S. (2018). M1-like macrophages change tumor blood vessels and microenvironment in murine melanoma. PLoS ONE 13, e0191012.

Kalucka, J., de Rooij, L.P.M.H., Goveia, J., Rohlenova, K., Dumas, S.J., Meta, E., Conchinha, N.V., Taverna, F., Teuwen, L.A., Veys, K., et al. (2020). Single-cell transcriptome atlas of murine endothelial cells. Cell 180, 764–779.e20.

Ke, X., Chen, C., Song, Y., Cai, Q., Li, J., Tang, Y., Han, X., Qu, W., Chen, A., Wang, H., et al. (2019). Hypoxia modifies the polarization of macrophages and their inflammatory microenvironment, and inhibits malignant behavior in cancer cells. Oncol. Lett. 18, 5871–5878.

Khodarev, N.N., Yu, J., Labay, E., Darga, T., Brown, C.K., Mauceri, H.J., Yassari, R., Gupta, N., and Weichselbaum, R.R. (2003). Tumour-endothelium interactions in co-culture: coordinated changes of gene expression profiles and phenotypic properties of endothelial cells. J. Cell Sci. 116, 1013–1022.

Kim, M.J., Sun, H.J., Song, Y.S., Yoo, S.K., Kim, Y.A., Seo, J.S., Park, Y.J., and Cho, S.W. (2019). CXCL16 positively correlated with M2-macrophage infiltration, enhanced angiogenesis, and poor prognosis in thyroid cancer. Sci. Rep. 9, 13288.

Kofler, N.M., Cuervo, H., Uh, M.K., Murtomäki, A., and Kitajewski, J. (2015). Combined deficiency of Notch1 and Notch3 causes pericyte dysfunction, models CADASIL, and results in arteriovenous malformations. Sci. Rep. 5, 16449.

Kothari, A.N., Arffa, M.L., Chang, V., Blackwell, R.H., Syn, W.K., Zhang, J., Mi, Z., and Kuo, P.C. (2016). Osteopontin-A master regulator of epithelial-mesenchymal transition. J. Clin. Med. 5, 39.

Kraan, J., van den Broek, P., Verhoef, C., Grunhagen, D.J., Taal, W., Gratama, J.W., and Sleijfer, S. (2014). Endothelial CD276 (B7-H3) expression is increased in human malignancies and distinguishes between normal and tumour-derived circulating endothelial cells. Br. J. Cancer 111, 149–156.

Krishnan, H., Rayes, J., Miyashita, T., Ishii, G., Retzbach, E.P., Sheehan, S.A., Takemoto, A., Chang, Y.W., Yoneda, K., Asai, J., et al. (2018). Podoplanin: an emerging cancer biomarker and therapeutic target. Cancer Sci. 109, 1292–1299.

Kuczynski, E.A., Yin, M., Bar-Zion, A., Lee, C.R., Butz, H., Man, S., Daley, F., Vermeulen, P.B., Yousef, G.M., Foster, F.S., et al. (2016). Co-option of liver vessels and not sprouting angiogenesis drives acquired sorafenib resistance in hepatocellular carcinoma. J. Natl. Cancer Inst. 108, djw030.

Kuczynski, E.A., Vermeulen, P.B., Pezzella, F., Kerbel, R.S., and Reynolds, A.R. (2019). Vessel co-option in cancer. Nat. Rev. Clin. Oncol. 16, 469–493.

Lan, J., Sun, L., Xu, F., Liu, L., Hu, F., Song, D., Hou, Z., Wu, W., Luo, X., Wang, J., et al. (2019). M2 Macrophage-derived exosomes promote cell migration and invasion in colon cancer. Cancer Res. *79*, 146–158.

Lazaris, A., Amri, A., Petrillo, S.K., Zoroquiain, P., Ibrahim, N., Salman, A., Gao, Z.H., Vermeulen, P.B., and Metrakos, P. (2018). Vascularization of colorectal carcinoma liver metastasis: insight into stratification of patients for anti-angiogenic therapies. J. Pathol. Clin. Res. *4*, 184–192.

Lee, W.S., Yang, H., Chon, H.J., and Kim, C. (2020). Combination of anti-angiogenic therapy and immune checkpoint blockade normalizes vascular-immune crosstalk to potentiate cancer immunity. Exp. Mol. Med. *52*, 1475–1485.

Leenders, W.P., Küsters, B., Verrijp, K., Maass, C., Wesseling, P., Heerschap, A., Ruiter, D., Ryan, A., and de Waal, R. (2004). Antiangiogenic therapy of cerebral melanoma metastases results in sustained tumor progression via vessel co-option. Clin. Cancer Res. *10*, 6222–6230.

Levandowsky, M., and Winter, D. (1971). Distance between sets. Nature *234*, 34.

Liu, P., Zhang, C., Chen, J., Zhang, R., Ren, J., Huang, Y., Zhu, F., Li, Z., and Wu, G. (2011). Combinational therapy of interferon-α and chemotherapy normalizes tumor vasculature by regulating pericytes including the novel marker RGS5 in melanoma. J. Immunother. *34*, 320–326.

Liu, J.Y., Jiang, L., Liu, J.J., He, T., Cui, Y.H., Qian, F., and Yu, P.W. (2018). AEBP1 promotes epithelial-mesenchymal transition of gastric cancer cells by activating the NF-κB pathway and predicts poor outcome of the patients. Sci. Rep. *8*, 11955.

Lopes-Bastos, B.M., Jiang, W.G., and Cai, J. (2016). Tumour-endothelial cell communications: important and indispensable mediators of tumour angiogenesis. Anticancer Res. *36*, 1119–1126.

Lu, L., Li, Z.J., Li, L.F., Wu, W.K., Shen, J., Zhang, L., Chan, R.L., Yu, L., Liu, Y.W., Ren, S.X., et al. (2015). Vascular-targeted TNFα improves tumor blood vessel function and enhances antitumor immunity and chemotherapy in colorectal cancer. J. Control. Release *210*, 134–146.

Lucio-Eterovic, A.K., Piao, Y., and de Groot, J.F. (2009). Mediators of glioblastoma resistance and invasion during antivascular endothelial growth factor therapy. Clin. Cancer Res. *15*, 4589–4599.

Luecken, M.D., and Theis, F.J. (2019). Current best practices in single-cell RNA-seq analysis: a tutorial. Mol. Syst. Biol. *15*, e8746.

Madden, E., Logue, S.E., Healy, S.J., Manie, S., and Samali, A. (2019). The role of the unfolded protein response in cancer progression: From oncogenesis to chemoresistance. Biol. Cell *111*, 1–17.

Mazzone, M., and Bergers, G. (2019). Regulation of blood and lymphatic vessels by immune cells in tumors and metastasis. Annu. Rev. Physiol. *81*, 535–560.

Moore, E.C., Sun, L., Clavijo, P.E., Friedman, J., Harford, J.B., Saleh, A.D., Van Waes, C., Chang, E.H., and Allen, C.T. (2018). Nanocomplex-based *TP53* gene therapy promotes anti-tumor immunity through TP53- and STING-dependent mechanisms. OncoImmunology *7*, e1404216.

Moraes, L.A., Ampomah, P.B., and Lim, L.H.K. (2018). Annexin A1 in inflammation and breast cancer: a new axis in the tumor microenvironment. Cell Adhes. Migr. *12*, 417–423.

Murray, L.A., Chen, Q., Kramer, M.S., Hesson, D.P., Argentieri, R.L., Peng, X., Gulati, M., Homer, R.J., Russell, T., van Rooijen, N., et al. (2011). TGF-beta driven lung fibrosis is macrophage dependent and blocked by Serum amyloid P. Int. J. Biochem. Cell Biol. *43*, 154–162.

Nielsen, S.R., and Schmid, M.C. (2017). Macrophages as key drivers of cancer progression and metastasis. Mediators Inflamm. *2017*, 9624760.

Noman, M.Z., Desantis, G., Janji, B., Hasmim, M., Karray, S., Dessen, P., Bronte, V., and Chouaib, S. (2014). PD-L1 is a novel direct target of HIF-1α, and its blockade under hypoxia enhanced MDSC-mediated T cell activation. J. Exp. Med. *211*, 781–790.

Pàez-Ribes, M., Allen, E., Hudock, J., Takeda, T., Okuyama, H., Viñals, F., Inoue, M., Bergers, G., Hanahan, D., and Casanovas, O. (2009). Antiangiogenic therapy elicits malignant progression of tumors to increased local invasion and distant metastasis. Cancer Cell *15*, 220–231.

Petrova, K., Oyadomari, S., Hendershot, L.M., and Ron, D. (2008). Regulated association of misfolded endoplasmic reticulum lumenal proteins with P58/DNAJc3. EMBO J. *27*, 2862–2872.

Pezzella, F., Pastorino, U., Tagliabue, E., Andreola, S., Sozzi, G., Gasparini, G., Menard, S., Gatter, K.C., Harris, A.L., Fox, S., et al. (1997). Non-small-cell lung carcinoma tumor growth without morphological evidence of neo-angiogenesis. Am. J. Pathol. *151*, 1417–1423.

Porcellini, S., Asperti, C., Valentinis, B., Tiziano, E., Mangia, P., Bordignon, C., Rizzardi, G.P., and Traversari, C. (2015). The tumor vessel targeting agent NGR-TNF controls the different stages of the tumorigenic process in transgenic mice by distinct mechanisms. OncoImmunology *4*, e1041700.

Potente, M., Gerhardt, H., and Carmeliet, P. (2011). Basic and therapeutic aspects of angiogenesis. Cell *146*, 873–887.

Pugh, C.W., and Ratcliffe, P.J. (2003). Regulation of angiogenesis by hypoxia: role of the HIF system. Nat. Med. *9*, 677–684.

Puram, S.V., Tirosh, I., Parikh, A.S., Patel, A.P., Yizhak, K., Gillespie, S., Rodman, C., Luo, C.L., Mroz, E.A., Emerick, K.S., et al. (2017). Single-cell transcriptomic analysis of primary and metastatic tumor ecosystems in head and neck cancer. Cell *171*, 1611–1624.e1624.

Pyonteck, S.M., Akkari, L., Schuhmacher, A.J., Bowman, R.L., Sevenich, L., Quail, D.F., Olson, O.C., Quick, M.L., Huse, J.T., Teijeiro, V., et al. (2013). CSF-1R inhibition alters macrophage polarization and blocks glioma progression. Nat. Med. *19*, 1264–1272.

Qian, J., Olbrecht, S., Boeckx, B., Vos, H., Laoui, D., Etlioglu, E., Wauters, E., Pomella, V., Verbandt, S., Busschaert, P., et al. (2020). A pan-cancer blueprint of the heterogeneous tumor microenvironment revealed by single-cell profiling. Cell Res. *30*, 745–762.

Rahat, M.A., Bitterman, H., and Lahat, N. (2011). Molecular mechanisms regulating macrophage response to hypoxia. Front. Immunol. *2*, 45.

Rey, S., Schito, L., Wouters, B.G., Eliasof, S., and Kerbel, R.S. (2017). Targeting hypoxia-inducible factors for antiangiogenic cancer therapy. Trends Cancer *3*, 529–541.

Ribatti, D., Nico, B., and Crivellato, E. (2011). The role of pericytes in angiogenesis. Int. J. Dev. Biol. *55*, 261–268.

Ritchie, M.E., Phipson, B., Wu, D., Hu, Y., Law, C.W., Shi, W., and Smyth, G.K. (2015). limma powers differential expression analyses for RNA-sequencing and microarray studies. Nucleic Acids Res. *43*, e47.

Rocha, S.F., Schiller, M., Jing, D., Li, H., Butz, S., Vestweber, D., Biljes, D., Drexler, H.C., Nieminen-Kelhä, M., Vajkoczy, P., et al. (2014). Esm1 modulates endothelial tip cell behavior and vascular permeability by enhancing VEGF bioavailability. Circ. Res. *115*, 581–590.

Rodvold, J.J., Mahadevan, N.R., and Zanetti, M. (2012). Lipocalin 2 in cancer: when good immunity goes bad. Cancer Lett. *316*, 132–138.

Rohlenova, K., Goveia, J., García-Caballero, M., Subramanian, A., Kalucka, J., Treps, L., Falkenberg, K.D., de Rooij, L.P.M.H., Zheng, Y., Lin, L., et al. (2020). Single-cell RNA sequencing maps endothelial metabolic plasticity in pathological angiogenesis. Cell Metab. *31*, 862–877.e14.

Rolny, C., Mazzone, M., Tugues, S., Laoui, D., Johansson, I., Coulon, C., Squadrito, M.L., Segura, I., Li, X., Knevels, E., et al. (2011). HRG inhibits tumor growth and metastasis by inducing macrophage polarization and vessel normalization through downregulation of PlGF. Cancer Cell *19*, 31–44.

Saiki, I., Fujii, H., Yoneda, J., Abe, F., Nakajima, M., Tsuruo, T., and Azuma, I. (1993). Role of aminopeptidase N (CD13) in tumor-cell invasion and extracellular matrix degradation. Int. J. Cancer *54*, 137–143.

Sakariassen, P.O., Prestegarden, L., Wang, J., Skaftnesmo, K.O., Mahesparan, R., Molthoff, C., Sminia, P., Sundlisaeter, E., Misra, A., Tysnes, B.B., et al. (2006). Angiogenesis-independent tumor growth mediated by stem-like cancer cells. Proc. Natl. Acad. Sci. USA *103*, 16466–16471.

Sardari Nia, P., Hendriks, J., Friedel, G., Van Schil, P., and Van Marck, E. (2007). Distinct angiogenic and non-angiogenic growth patterns of lung metastases from renal cell carcinoma. Histopathology *51*, 354–361.

Satija, R., Farrell, J.A., Gennert, D., Schier, A.F., and Regev, A. (2015). Spatial reconstruction of single-cell gene expression data. Nat. Biotechnol. *33*, 495–502.

Schmittnaegel, M., Rigamonti, N., Kadioglu, E., Cassará, A., Wyser Rmili, C., Kiialainen, A., Kienast, Y., Mueller, H.J., Ooi, C.H., Laoui, D., and De Palma, M. (2017). Dual angiopoietin-2 and VEGFA inhibition elicits antitumor immunity that is enhanced by PD-1 checkpoint blockade. Sci. Transl. Med. *9*, eaak9670.

Seaman, S., Zhu, Z., Saha, S., Zhang, X.M., Yang, M.Y., Hilton, M.B., Morris, K., Szot, C., Morris, H., Swing, D.A., et al. (2017). Eradication of tumors through simultaneous ablation of CD276/B7-H3-positive tumor cells and tumor vasculature. Cancer Cell *31*, 501–515.e8.

Shaheen, R.M., Tseng, W.W., Davis, D.W., Liu, W., Reinmuth, N., Vellagas, R., Wieczorek, A.A., Ogura, Y., McConkey, D.J., Drazan, K.E., et al. (2001). Tyrosine kinase inhibition of multiple angiogenic growth factor receptors improves survival in mice bearing colon cancer liver metastases by inhibition of endothelial cell survival mechanisms. Cancer Res. *61*, 1464–1468.

Shojaei, F., Wu, X., Malik, A.K., Zhong, C., Baldwin, M.E., Schanz, S., Fuh, G., Gerber, H.P., and Ferrara, N. (2007). Tumor refractoriness to anti-VEGF treatment is mediated by CD11b⁺Gr1⁺ myeloid cells. Nat. Biotechnol. *25*, 911–920.

Shojaei, F., Wu, X., Qu, X., Kowanetz, M., Yu, L., Tan, M., Meng, Y.G., and Ferrara, N. (2009). G-CSF-initiated myeloid cell mobilization and angiogenesis mediate tumor refractoriness to anti-VEGF therapy in mouse models. Proc. Natl. Acad. Sci. USA *106*, 6742–6747.

Simonavicius, N., Robertson, D., Bax, D.A., Jones, C., Huijbers, I.J., and Isacke, C.M. (2008). Endosialin (CD248) is a marker of tumor-associated pericytes in high-grade glioma. Mod. Pathol. *21*, 308–315.

Smillie, C.S., Biton, M., Ordovas-Montanes, J., Sullivan, K.M., Burgin, G., Graham, D.B., Herbst, R.H., Rogel, N., Slyper, M., Waldman, J., et al. (2019). Intra- and inter-cellular rewiring of the human colon during ulcerative colitis. Cell *178*, 714–730.e22.

Solinas, G., Schiarea, S., Liguori, M., Fabbri, M., Pesce, S., Zammataro, L., Pasqualini, F., Nebuloni, M., Chiabrando, C., Mantovani, A., and Allavena, P. (2010). Tumor-conditioned macrophages secrete migration-stimulating factor: a new marker for M2-polarization, influencing tumor cell motility. J. Immunol. *185*, 642–652.

Song, S., Ewald, A.J., Stallcup, W., Werb, Z., and Bergers, G. (2005). PDGFRβ⁺ perivascular progenitor cells in tumours regulate pericyte differentiation and vascular survival. Nat. Cell Biol. *7*, 870–879.

Song, Q., Hawkins, G.A., Wudel, L., Chou, P.C., Forbes, E., Pullikuth, A.K., Liu, L., Jin, G., Craddock, L., Topaloglu, U., et al. (2019). Dissecting intratumoral myeloid cell plasticity by single cell RNA-seq. Cancer Med. *8*, 3072–3085.

Stapor, P.C., Sweat, R.S., Dashti, D.C., Betancourt, A.M., and Murfee, W.L. (2014). Pericyte dynamics during angiogenesis: new insights from new identities. J. Vasc. Res. *51*, 163–174.

Stessels, F., Van den Eynden, G., Van der Auwera, I., Salgado, R., Van den Heuvel, E., Harris, A.L., Jackson, D.G., Colpaert, C.G., van Marck, E.A., Dirix, L.Y., and Vermeulen, P.B. (2004). Breast adenocarcinoma liver metastases, in contrast to colorectal cancer liver metastases, display a non-angiogenic growth pattern that preserves the stroma and lacks hypoxia. Br. J. Cancer *90*, 1429–1436.

Storey, J.D., Bass, A.J., Dabney, A., Robinson, D., and Warnes, G. (2015). qvalue: Q-value estimation for false discovery rate control. (R Foundation for Statistical Computing), R package version 2.10.0.

Suzuki, R., and Shimodaira, H. (2006). Pvclust: an R package for assessing the uncertainty in hierarchical clustering. Bioinformatics *22*, 1540–1542.

Szulzewsky, F., Pelz, A., Feng, X., Synowitz, M., Markovic, D., Langmann, T., Holtman, I.R., Wang, X., Eggen, B.J., Boddeke, H.W., et al. (2015). Glioma-associated microglia/macrophages display an expression profile different from M1 and M2 polarization and highly express Gpnmb and Spp1. PLoS ONE *10*, e0116644.

Tabula Muris Consortium; Overall coordination; Logistical coordination; Organ collection and processing; Library preparation and sequencing; Computational data analysis; Cell type annotation; Writing group; Supplemental text writing group; Principal investigators (2018). Single-cell transcriptomics of 20 mouse organs creates a Tabula Muris. Nature *562*, 367–372.

Takeda, N., O'Dea, E.L., Doedens, A., Kim, J.W., Weidemann, A., Stockmann, C., Asagiri, M., Simon, M.C., Hoffmann, A., and Johnson, R.S. (2010). Differential activation and antagonistic function of HIF-alpha isoforms in macrophages are essential for NO homeostasis. Genes Dev. *24*, 491–501.

Taverna, F., Goveia, J., Karakach, T.K., Khan, S., Rohlenova, K., Treps, L., Subramanian, A., Schoonjans, L., Dewerchin, M., Eelen, G., and Carmeliet, P. (2020). BIOMEX: an interactive workflow for (single cell) omics data interpretation and visualization. Nucleic Acids Res. *48* (*W1*), W385–W394.

Tazzyman, S., Niaz, H., and Murdoch, C. (2013). Neutrophil-mediated tumour angiogenesis: subversion of immune responses to promote tumour growth. Semin. Cancer Biol. *23*, 149–158.

Teicher, B.A. (2019). CD248: a therapeutic target in cancer and fibrotic diseases. Oncotarget *10*, 993–1009.

Uhlén, M., Fagerberg, L., Hallström, B.M., Lindskog, C., Oksvold, P., Mardinoglu, A., Sivertsson, Å., Kampf, C., Sjöstedt, E., Asplund, A., et al. (2015). Proteomics: tissue-based map of the human proteome. Science *347*, 1260419.

Valiente, M., Obenauf, A.C., Jin, X., Chen, Q., Zhang, X.H., Lee, D.J., Chaft, J.E., Kris, M.G., Huse, J.T., Brogi, E., and Massagué, J. (2014). Serpins promote cancer cell survival and vascular co-option in brain metastasis. Cell *156*, 1002–1016.

van Dalen, F.J., van Stevendaal, M.H.M.E., Fennemann, F.L., Verdoes, M., and Ilina, O. (2018). Molecular repolarisation of tumour-associated macrophages. Molecules *24*, 9.

Van de Veire, S., Stalmans, I., Heindryckx, F., Oura, H., Tijeras-Raballand, A., Schmidt, T., Loges, S., Albrecht, I., Jonckx, B., Vinckier, S., et al. (2010). Further pharmacological and genetic evidence for the efficacy of PlGF inhibition in cancer and eye disease. Cell *141*, 178–190.

van den Brink, S.C., Sage, F., Vértesy, Á., Spanjaard, B., Peterson-Maduro, J., Baron, C.S., Robin, C., and van Oudenaarden, A. (2017). Single-cell sequencing reveals dissociation-induced gene expression in tissue subpopulations. Nat. Methods *14*, 935–936.

van der Maaten, L.J.P., and Hinton, G.E. (2008). Visualizing high-dimensional data using t-SNE. J. Mach. Learn. Res. *9*, 2579–2605.

Vanlandewijck, M., He, L., Mäe, M.A., Andrae, J., Ando, K., Del Gaudio, F., Nahar, K., Lebouvier, T., Laviña, B., Gouveia, L., et al. (2018). A molecular atlas of cell types and zonation in the brain vasculature. Nature *554*, 475–480.

Vasudev, N.S., and Reynolds, A.R. (2014). Anti-angiogenic therapy for cancer: current progress, unresolved questions and future directions. Angiogenesis *17*, 471–494.

Vermeulen, P.B., Colpaert, C., Salgado, R., Royers, R., Hellemans, H., Van Den Heuvel, E., Goovaerts, G., Dirix, L.Y., and Van Marck, E. (2001). Liver metastases from colorectal adenocarcinomas grow in three patterns with different angiogenesis and desmoplasia. J. Pathol. *195*, 336–342.

Vizovišek, M., Fonović, M., and Turk, B. (2019). Cysteine cathepsins in extracellular matrix remodeling: Extracellular matrix degradation and beyond. Matrix Biol. *75-76*, 141–159.

Wallin, J.J., Bendell, J.C., Funke, R., Sznol, M., Korski, K., Jones, S., Hernandez, G., Mier, J., He, X., Hodi, F.S., et al. (2016). Atezolizumab in combination with bevacizumab enhances antigen-specific T-cell migration in metastatic renal cell carcinoma. Nat. Commun. *7*, 12624.

Wang, J., Lee, J., Liem, D., and Ping, P. (2017). HSPA5 gene encoding Hsp70 chaperone BiP in the endoplasmic reticulum. Gene *618*, 14–23.

Wang, D.W., Zheng, H.Z., Cha, N., Zhang, X.J., Zheng, M., Chen, M.M., and Tian, L.X. (2020). Down-regulation of AHNAK2 inhibits cell proliferation, migration and invasion through inactivating the MAPK pathway in lung adenocarcinoma. Technol. Cancer Res. Treat. *19*, 1533033820957006.

Wen, Q., Han, T., Wang, Z., and Jiang, S. (2020). Role and mechanism of programmed death-ligand 1 in hypoxia-induced liver cancer immune escape. Oncol. Lett. *19*, 2595–2601.

Winkler, E.A., Bell, R.D., and Zlokovic, B.V. (2011). Central nervous system pericytes in health and disease. Nat. Neurosci. *14*, 1398–1405.

Wyckoff, J., Wang, W., Lin, E.Y., Wang, Y., Pixley, F., Stanley, E.R., Graf, T., Pollard, J.W., Segall, J., and Condeelis, J. (2004). A paracrine loop between tumor cells and macrophages is required for tumor cell migration in mammary tumors. Cancer Res. *64*, 7022–7029.

Xie, T., Wang, Y., Deng, N., Huang, G., Taghavifar, F., Geng, Y., Liu, N., Kulur, V., Yao, C., Chen, P., et al. (2018). Single-cell deconvolution of fibroblast heterogeneity in mouse pulmonary fibrosis. Cell Rep. *22*, 3625–3640.

Xu, C., Bailly-Maitre, B., and Reed, J.C. (2005). Endoplasmic reticulum stress: cell life and death decisions. J. Clin. Invest. *115*, 2656–2664.

Yamazaki, T., and Mukouyama, Y.S. (2018). Tissue specific origin, development, and pathological perspectives of pericytes. Front. Cardiovasc. Med. *5*, 78.

Yang, L., DeBusk, L.M., Fukuda, K., Fingleton, B., Green-Jarvis, B., Shyr, Y., Matrisian, L.M., Carbone, D.P., and Lin, P.C. (2004). Expansion of myeloid immune suppressor Gr$^+$CD11b$^+$ cells in tumor-bearing host directly promotes tumor angiogenesis. Cancer Cell *6*, 409–421.

Yokoi, K., Sasaki, T., Bucana, C.D., Fan, D., Baker, C.H., Kitadai, Y., Kuwai, T., Abbruzzese, J.L., and Fidler, I.J. (2005). Simultaneous inhibition of EGFR, VEGFR, and platelet-derived growth factor receptor signaling combined with gemcitabine produces therapy of human pancreatic carcinoma and prolongs survival in an orthotopic nude mouse model. Cancer Res. *65*, 10371–10380.

Zhang, S., Lu, Y., Qi, L., Wang, H., Wang, Z., and Cai, Z. (2020). AHNAK2 is associated with poor prognosis and cell migration in lung adenocarcinoma. BioMed Res. Int. *2020*, 8571932.

Zhu, Y., Knolhoff, B.L., Meyer, M.A., Nywening, T.M., West, B.L., Luo, J., Wang-Gillam, A., Goedegebuure, S.P., Linehan, D.C., and DeNardo, D.G. (2014). CSF1/CSF1R blockade reprograms tumor-infiltrating macrophages and improves response to T-cell checkpoint immunotherapy in pancreatic cancer models. Cancer Res. *74*, 5057–5069.

STAR★METHODS

KEY RESOURCES TABLE

REAGENT or RESOURCE	SOURCE	IDENTIFIER
Antibodies		
Rabbit anti-mouse CD34	BD Biosciences	Cat# BD553731; RRID: AB_395015
Goat anti-mouse ESM1	R&D	Cat# AF 1999; RRID: AB_2101810
Rat anti-mouse CD31	BD Biosciences	Cat# 550274; RRID: AB_393571
Hamster anti-mouse PDPN	DSHB	Cat# 8.1.1; RRID: AB_531893
Rabbit anti-mouse PDGFRB	Abcam	Cat# ab32570; RRID: AB_777165
Rat anti-mouse F4/80	Serotec	Cat# MCA497; RRID: AB_2098196
Rabbit anti-mouse CD80	Abcam	Cat# ab64116; RRID: AB_1640342
Rabbit anti-mouse GPNMB	Bioss	Cat# bs-2684R; RRID:AB_10855152
Rabbit anti-mouse FXYD2	Proteintech	Cat# 11198-1-AP; RRID: AB_2108309
Goat anti-mouse SPARC	R&D	Cat# AF942; RRID: AB_2286625
Prolong Gold Antifade Mountant	Thermo Fisher Scientific	Cat# P36934; RRID: AB_2315602
Biological samples		
RENCA lung metastasis samples (study approved by the Animal Ethics Committee of the KU Leuven under protocol number P084/2016)	This paper	N/A
Chemicals, peptides, and recombinant proteins		
Antibiotic/antimycotic	Thermo Fisher Scientific	15240062
Benzyl alcohol	Sigma-Aldrich	402834
Bovine serum albumin (BSA)	Sigma-Aldrich	A2058
Bovine serum albumin (UltraPure BSA)	Thermo Fisher Scientific	AM2616
Carboxymethylcellulose sodium	Sigma-Aldrich	C9481
Click-iT™ Plus EdU Cell Proliferation Kit for Imaging	Thermo Fisher Scientific	A20187
Collagenase II	Thermo Fisher Scientific	GIBCO™17101015
Collagenase IV	Worthington Biochemical	LS004188
DMEM	Thermo Fisher Scientific	11965-084
DNase I	Sigma-Aldrich	D4527
ECGS/H (endothelial cell growth supplement/heparin)	Bio-Connect	PromoCell C-39216
EDTA	VWR Chemicals	20302.293
EdU (5-ethynyl-2′-deoxyuridine)	Thermo Fisher Scientific	A10044
Fetal bovine serum (FBS)	Merck - Biochrom	S 0415
Glutamine	Thermo Fisher Scientific	25030149
Hoechst 33258	Sigma-Aldrich	B2261
Hypoxyprobe™ kit	Chemicon-Millipore	HP1-XXX
MEM NEAAs	Thermo Fisher Scientific	11140035
Nimatek (100mg/mL); Ketamine	Dechra	N/A
Penicillin/Streptomycin	Thermo Fisher Scientific	15140122
Phosphate buffered saline (PBS)	Thermo Fisher Scientific	14190094
ROTI® Histofix 4%	Carl Roth	P087.1
RPMI 1640	Thermo Fisher Scientific	21875-034
Sodium pyruvate	Thermo Fisher Scientific	11360070
Sunitinib, Malate Salt	LC laboratories	S-8803
Tween 80	Sigma-Aldrich	P1754
VivoGlo™ Luciferin, *In Vivo* Grade	Promega	P1041
Xylazine	VMD	XYL-M 2%

(Continued on next page)

Continued

REAGENT or RESOURCE	SOURCE	IDENTIFIER
Critical commercial assays		
CD31 MicroBeads, mouse	Miltenyi Biotec	130-097-418
CD45 MicroBeads, mouse	Miltenyi Biotec	130-052-301
CD326 MicroBeads, mouse	Miltenyi Biotec	130-105-958
Chromium Single Cell 3′ Library, Gel Bead & Multiplex Kit and Chip Kit, v2	10x Genomics	PN-120237
Chromium Single Cell A Chip Kit	10x Genomics	PN-120236
Chromium i7 Multiplex Kit	10x Genomics	PN-120262
RNAscope Multiplex Fluorescent v2 Assay	ACDBio	323110
TSA Cyanine 3 (Cy3) System	Perkin Elmer	NEL704A001KT
TSA Cyanine 5 (Cy5) System	Perkin Elmer	NEL705A001KT
TSA Fluorescein System	Perkin Elmer	NEL701A001KT
Deposited data		
RNA-sequencing raw data mouse EC	This paper	ArrayExpress: E-MTAB-9227
LLC scRNA-seq dataset	Goveia et al., 2020	ArrayExpress: E-MTAB-7458
Mouse lung development scRNA-seq dataset	Cohen et al., 2018	NCBI Gene Expression Omnibus: GSE119228
Tabula muris scRNA-seq dataset	Tabula Muris Consortium et al., 2018	NCBI Gene Expression Omnibus: GSE109774
Mouse lung vascular scRNA-seq dataset	He et al., 2018b	NCBI Gene Expression Omnibus: GSE99235
Experimental models: Cell lines		
Luciferase-tagged 4T1 cells	A. Reynolds	N/A
Luciferase-tagged RENCA cells	A. Reynolds	N/A
Experimental models: Organisms/strains		
BALB/c mice	KU Leuven animal facility	N/A
BALB/c mice	Charles Rivers	N/A
Oligonucleotides		
RNAscope probe Mm-Actg2	ACDBio	483811
RNAscope probe Mm-Rgs5	ACDBio	430181
RNAscope Probe 3-plex Positive Control Probe_Mm	ACDBio	320881
RNAscope Probe 3-plex Negative Control Probe	ACDBio	320871
Software and algorithms		
R version 3.4.4 (2018-03-15) system: x86_64, mingw32, ui: RStudio (1.1.456), language: (EN), collate: English United States.1252	CRAN (R 3.4.4)	N/A
Cell Ranger	10x Genomics	(tenx, RRID: SCR_01695)
clusterProfiler; version 3.6.0	Bioconductor	(clusterProfiler, RRID: SCR_016884
flashPCA; version 2	https://github.com/gabraham/flashpca	N/A
Gorilla, version February 7, 2020	http://cbl-gorilla.cs.technion.ac.il	(Gorilla, RRID: SCR_006848)
GSVA; version 1.26.0	Bioconductor	N/A
heatmaply; version 0.16.0	CRAN (R 3.4.4)	N/A
limma; version 0.16.0	Bioconductor	(LIMMMA, RRID: SCR_010943)
org.Mm.eg.db; version 3.5.0	Bioconductor	N/A
plotly; version 4.8.0.9000	Github (ropensci/plotly@f43699e)	(plotly, RRID: SCR_013991)
pvclust; version 2.0.0	CRAN (R 3.4.4)	N/A

(Continued on next page)

Continued

REAGENT or RESOURCE	SOURCE	IDENTIFIER
qvalue; version 2.10.0	Bioconductor	(Qvalue, RRID: SCR_001073)
Rtsne; version 0.15	CRAN (R 3.4.4)	N/A
scran; version 1.6.9	Bioconductor	(scran, RRID: SCR_016944)
Seurat; version 2.3.4	CRAN (R 3.4.4)	(Seurat, RRID: SCR_016341)
GraphPad Prism8, version 8.1.1		(GraphPad Prism, RRID: SCR_002798)
Fiji/ImageJ, 1.52n	https://fiji.sc	RRID: SCR_002285
Living Image software (version 4.4.17504)	PerkinElmer	(Living Image software, RRID: SCR_014247)
Other		
40 μm cell strainer	Sigma-Aldrich	CLS431750
GentleMACS C tubes	Miltenyi Biotec	130-093-237
LS columns	Miltenyi Biotec	130-042-401
MS columns	Miltenyi Biotec	130-042-201

RESOURCE AVAILABILITY

Lead contact
Correspondence and requests for materials should be addressed to the lead contact, Peter Carmeliet (peter.carmeliet@kuleuven.be).

Materials availability
This study did not generate new unique reagents.

Data and code availability
All raw sequencing data generated during this study are available at ArrayExpress. The accession number for the data reported in this paper is ArrayExpress: E-MTAB-9227. Publicly available single cell transcriptome data were derived from ArrayExpress (accession number E-MTAB-7458) and from Gene Expression Omnibus (accession numbers GSE109774, GSE119228 and GSE99235). The published article includes all data generated or analyzed during this study.

EXPERIMENTAL MODEL AND SUBJECT DETAILS

Animals
Experiments were performed in 8 to 10 week-old female immunocompetent BALB/c mice (obtained from KU Leuven animal facility or purchased from Charles River Laboratories) that had not been involved in previous procedures. Animals were housed in individually ventilated cages in a room with controlled temperature and humidity under a 12 h light / 12 h dark cycle with access to food and water *ad libitum*. Animals were closely followed-up by the experimenters and animal caretakers, with regular inspection by a veterinarian, as per standard health and animal welfare procedures of the local animal facility. No statistical method was used to predetermine sample size. Animals were randomly allocated to experimental groups, balanced for body weight. Animal housing and all experimental procedures were approved by the Institutional Animal Ethics Committee of the KU Leuven (Belgium) under protocol number P084/2016.

Cell Lines
RENCA and 4T1 Cells
The Luciferase-tagged 'RENCA' renal cancer cell line and '4T1' breast cancer cell line were a gift from Andrew R. Reynolds, Cambridge. Cells were cultured at 37°C, 5% CO_2 in RPMI 1640 (Thermo Fisher Scientific) supplemented with 10% fetal bovine serum (Merck - Biochrom), 2 mM L-glutamine (Thermo Fisher Scientific), 100 IU/mL penicillin and 100 mg/mL streptomycin (Thermo Fisher Scientific). Cell lines were checked for mycoplasma and were contamination free.

METHOD DETAILS

Mouse model of renal cancer experimental lung metastasis
RENCA cells were cultured for at least 2 passages and injected into the tail vein of the mice using a 29G needle (2×10^5 cells in 0.1 mL phosphate buffered saline (PBS)) (Bridgeman et al., 2017). The animals were sacrificed on day 10, day 21 or day 36 of the experiment and lungs were immediately processed for metastatic cell or EC isolation.

Mouse model of breast cancer experimental lung metastasis

4T1 cells were cultured for at least 2 passages and injected into the tail vein of the mice using a 29G needle (2×10^5 cells in 0.1 mL PBS) (Bridgeman et al., 2017). The animals were sacrificed on day 13 of the experiment and lungs were immediately processed for histology.

Sunitinib treatment

Mice were treated with Sunitinib (LC laboratories) (40 mg/kg dissolved in control vehicle, every day), or with a control vehicle (0.5% carboxymethylcellulose sodium, 1.8% w/v NaCl, 0.4% w/v Tween 80, 0.9% w/v benzyl alcohol dissolved in reverse osmosis deionized water adjusted to pH 6) by daily gavage of 0.2 mL (Bridgeman et al., 2017). For the RENCA model, treatment started from day 10 after injection of RENCA cells and continued until day 20 (Bridgeman et al., 2017) or day 35. For the 4T1 model, treatment started from day 3 after injection of 4T1 cells and continued for 10 days (Bridgeman et al., 2017). Mice were randomly allocated to the treatment condition, balanced for body weight.

Metastatic cell isolation & tumor and normal endothelial cell isolation

For metastatic cells and TECs, mice were anesthetized and killed via cervical dislocation, lungs were dissected and per mouse, at least 60 metastases were micro-dissected under a dissection microscope. For NECs, control (non-tumor bearing) mice were anesthetized with an intraperitoneal injection of ketamine (100 mg/kg body weight) and xylazine (10 mg/kg body weight), lungs were perfused with 5 mL PBS at 120 mL/h and both lungs were dissected. The dissected tissue was placed into a GentleMACS C Tube (Miltenyi Biotec) containing 5 mL of digestion buffer on ice (0.1% collagenase II (Thermo Fisher Scientific), 0.25% collagenase IV (Worthington Biochemical) and DNase I (15 μM) in DMEM supplemented with 1x sodium pyruvate, 1x MEM NEAAs, ECGF/Heparin, antibiotic/antimycotic (2x) and 1% penicillin/streptomycin (Thermo Fisher Scientific)). The dissected tissues were dissociated using the gentleMACS™ Dissociator (Miltenyi Biotec; on m_lung_01 protocol) and incubated in a water bath at 37°C for 30 min with manual shaking every 5 min. At the end of the tissue digestion process, the samples were again placed in the gentleMACS™ Dissociator (Miltenyi Biotec; on m_lung_02 protocol) and the reaction was stopped by adding 10 mL of an isolation buffer containing PBS, 0.5% BSA and 40 mM EDTA. Subsequently, the cell suspension was filtered through a 40 μm cell strainer (Sigma-Aldrich) and cells were rinsed with isolation buffer. Next, for TECs and NECs, ECs were enriched by magnetic bead sorting using the MACS system (Miltenyi Biotec) at room temperature. First, immune cells and epithelial cells were depleted using selection with CD45 and CD326 MicroBeads (Miltenyi Biotec), followed by positive selection of ECs with CD31 MicroBeads (Miltenyi Biotec), using LS and MS columns (Miltenyi Biotec), according to the manufacturer's instructions. For further processing for scRNA-seq, the samples were resuspended in PBS containing 0.4% UltraPure BSA (50 mg/mL; Thermo Fisher Scientific) and filtered over 40 μm cell strainers on ice. Overall, it took between 3 to 4 h from obtaining metastases collection to obtaining single-cell EC suspensions. For metastatic cells, no selection procedure was applied and it took between 1 to 2 h from collecting metastases to generating single-cell metastatic cell suspensions. Viability was between 85%–94% and cells were kept on ice whenever possible.

Histology, immunohistochemistry and morphometric analysis
Histology and immunohistochemistry

All methods for histology and immunostainings have been described (Bridgeman et al., 2017; Cantelmo et al., 2016). Briefly, mice were perfused via the right heart ventricle with 10 mL PBS and 10 mL PFA 4% (Histofix, Carl Roth) and lungs were inflated with 0.5 mL PFA 4% via intratracheal injection. Lungs were fixed for 24 h in PFA 4% at 4°C, dehydrated, embedded in paraffin for 7μm serial sections and subjected to immunohistochemistry. For a full list of primary and secondary antibodies, see Key resources table. Briefly, after overnight incubation at room temperature with the primary antibodies, sections were incubated with the appropriate fluorescently conjugated secondary antibodies, followed by amplification with the proper tyramide signal amplification system (Perkin Elmer). Nuclei were counterstained with Hoechst 33342 (Sigma-Aldrich) and slides were mounted using Prolong Gold Antifade Mountant (Thermo Fisher Scientific). Imaging was performed using a Leica DMI 6000 B inverted microscope (Leica Microsystems) at 5x magnification, a Zeiss AxioScan Z1 microscope (Carl Zeiss) at 20x magnification, or by confocal imaging using a Zeiss LSM 780 confocal microscope (Carl Zeiss) at 40x magnification (EC Plan-Neofluar 40x/1.30 Oil DIC M27) or 100x magnification (alpha Plan-Apochromat 100x/1.46 Oil DIC M27). The images were processed using Fiji software (https://fiji.sc).

Morphometric analyses

MICROVESSEL DENSITY was measured as total CD34$^+$ area, expressed as a percentage of total tumor area. EC PROLIFERATION was analyzed using the Click-iT 5-ethynyl-2'-deoxyuridine (EdU) Alexa Fluor 555 Imaging Kit (Thermo Fisher Scientific) and was measured as the number of EdU$^+$ CD34$^+$ ECs, expressed as a percentage of the total number of CD34$^+$ ECs. TIP ECs were measured as the number of ESM1$^+$ CD34$^+$ ECs, expressed as a percentage per mm^2 of vessel area. TUMOR HYPOXIA was detected after injection of 60 mg/kg pimonidazole hydrochloride (Hypoxyprobe kit) into tumor-bearing mice (tumors were harvested 1 h after injection). To detect the formation of pimonidazole adducts, tumor paraffin sections were immunostained with Hypoxyprobe-1-Mab1 (Hypoxyprobe kit, Chemicon-Millipore) following the manufacturer's instructions. The hypoxic area was expressed as a percentage of the total metastatic area. DETERMINATION OF VASCULAR TYPE of lung metastases was executed as previously described (Bridgeman et al., 2017). Briefly, metastases were scored as 'pushing angiogenic' or 'interstitial vessel co-option' based on interpretation of

H&E staining and CD31-podoplanin staining. TUMOR BURDEN was assessed on hematoxylin and eosin (H&E) stained paraffin sections and the tumor area was expressed as a percentage of the total lung area.

RNAscope *in situ* hybridization and quantification

Formalin-fixed paraffin-embedded metastatic lung sections were subjected to RNAscope *in situ* hybridization using the RNAscope Multiplex Fluorescent v2 assay (ACDBio) according to the manufacturer's instructions (Pretreatment and RNAscope Multiplex Fluorescent v2 Assay according to protocol 323100-USM). Briefly, after deparaffinization, the slides were incubated with hydrogen peroxide for 10 min at room temperature. After several washing steps, manual target retrieval was performed followed by incubation with Protease Plus before proceeding to the RNAscope Multiplex Fluorescent v2 protocol. Hybridization was performed with the RNAscope probes Mm-Rgs5 (430181), Mm-Actg2 (483811), RNAscope Probe 3-plex Positive Control Probe_Mm (320881) and RNAscope Probe 3-plex Negative Control Probe (320871). Slides were then processed according to the RNAscope Multiplex Fluorescent v2 protocol (Hybridization, Amplification, and Signal Development), prior to immunohistochemical staining for CD34 (BD Biosciences, BD553731), PDGFRB (Abcam, AB32570) and nuclear staining (Hoechst 33342). Images were acquired using a Zeiss LSM 780 confocal microscope (Carl Zeiss). For quantification, number of transcripts in each PDGFRB$^+$ cell adjacent to a CD34$^+$ cell were manually counted. Results are depicted as number of dots per pericyte.

Bioluminescence imaging

In vivo bioluminescence imaging was carried out on an IVIS Spectrum System (CaliperLS; Perkin-Elmer) and luminescence was quantified with Living Image software (version 4.4.17504). Mice were injected intraperitoneally with D-luciferin (126 mg/kg dissolved in PBS (15 mg/mL)) and anesthetized with isoflurane gas. Immediately after substrate administration, acquisition of consecutive frames was initiated until maximum signal intensity was reached, covering a total of at least 10 minutes. Image acquisition numbers and times varied between 10 and 15 frames of 60 s each, depending on the optimal acquisition settings in function of the signal intensity intrinsic to the grade of lung metastases. Photon flux per second (p/s) was measured through a region of interest (2.9 cm × 1.9 cm) covering the lungs.

Single-cell droplet-based RNA sequencing

The single-cell suspensions of freshly isolated metastatic cells and ECs (MACS-bead enriched as described above) were resuspended in PBS with 0.04% ultra-pure BSA and converted to barcoded scRNA-seq libraries using the Chromium Single Cell 3′ Library, Gel Bead & Multiplex Kit and Chip Kit (10x Genomics), aiming for 6,000 cells per library. Samples were processed using kits pertaining to V2 barcoding chemistry of 10x Genomics. Single samples were always processed in a single well of a PCR plate, allowing all cells from a sample to be treated with the same master mix and in the same reaction vessel. Libraries were sequenced on an Illumina HiSeq4000, de-multiplexed, and mapped to the mouse genome (build mm10) using CellRanger software (10x Genomics, version 2.1.1).

Single-cell transcriptomics analysis

Data from the metastatic cell samples and the MACS-enriched TEC and NEC samples were aggregated using CellRanger software (10x Genomics, version 2.1.1) and data from the raw unfiltered matrix was further processed using R (version 3.4.4 - *Someone to Lean On*). Key quality metrics are listed in Table S1.

Quality control and data normalization

For the non-EC-enriched dataset, the following quality control steps were applied: (i) genes expressed by less than 20 cells and/or with a row mean of < 0.01 were excluded from further analysis; (ii) cells that expressed fewer than 300 genes (low quality), and cells that expressed over 7,000 genes (potential doublets) were removed; (iii) cells in which more than 10% of unique molecular identifiers (UMIs) were derived from the mitochondrial genome were not considered. Quality control of the EC-enriched dataset was performed using a similar approach, see Table S1 for dataset specific cut-off values and parameter settings. The data of the remaining cells were natural log-transformed (using log1p) and normalized using the *Seurat* package version 2.3.4 (Satija et al., 2015).

EC-enriched dataset: *in silico* endothelial cell and pericyte selection

All analyses were performed using the browser-based software BIOMEX (Taverna et al., 2020). For the EC-enriched dataset, data was auto-scaled, summarized by principal component analysis (PCA) using the *flash*PCA package (Abraham et al., 2017), and the first 15 PCAs were visualized using t-Distributed Stochastic Neighbor Embedding (t-SNE, *Rtsne* package [van der Maaten and Hinton, 2008]) with a perplexity of 200 and learning rate of 100. Using the *FindClusters* function in *Seurat*, graph-based clustering was performed to cluster cells according to their gene expression profile (clustering resolution = 0.5, k-nearest neighbors = 30). See Table S1 for details. Clusters were annotated based on the expression of canonical marker genes, including *Pecam1* and *Cdh5* (ECs), *Fxyd2* and *Chchd10* (cancer cells), *Ptprc* (leukocytes), *Mgp* and *Bgn* (mesenchymal cells), *Sftpa1*, *Sftpc* and *Ager* (pneumocytes). Contaminating cell clusters (non-ECs) were removed and downstream analysis was performed on ECs only.

Despite the EC enrichment procedure, a fraction of mesenchymal cells (including pericytes) was still present in the dataset. For pericyte analysis, all non-mesenchymal cells were removed and downstream analysis was performed on mesenchymal cells only.

EC-enriched dataset: batch effect correction

The EC-enriched dataset was sequenced in three separate batches. For the selected ECs and mesenchymal cells, we first analyzed each batch separately, and removed clusters expressing ambiguous marker genes (i.e., representing low quality cells, red blood cells, possible doublets, etc.), as performed in other scRNA-seq studies (Goveia et al., 2020; Smillie et al., 2019). To correct for batch effects, we used a recently developed algorithm, *mnnCorrect* available from the *scran* package (Haghverdi et al., 2018). The optimal neighborhood size, k, was empirically defined as 50 after optimizing over a range of 10-300.

EC-enriched dataset: feature selection and dimensionality reduction

After *in silico* cell selection and batch correction for joint analysis, we performed PCA on highly variable genes, detected using the *FindVariableGenes* function in *Seurat*. This function calculates the mean expression and dispersion for each gene, groups genes into bins (size 20) by their mean expression and identifies any gene for which the z-score calculated from the dispersion exceeds a pre-defined cut-off. For most experiments, we used a cut-off of z = 0.25 and mean expression in the range 0.000125 to 8, all other parameters were default (see Table S1 for parameter settings for each analysis). We then generated a t-SNE to construct a two-dimensional representation of the data. This representation was only used to visualize the data.

Non-EC enriched dataset: feature selection and dimensionality reduction

For the non-EC-enriched dataset, we first identified highly variable genes using the *Seurat FindVariableGenes* function (mean lower threshold = 0.125, mean higher threshold = 8, dispersion threshold = 0.25). Data was then auto-scaled, summarized by principal component analysis (PCA) using the *flash*PCA package (Abraham et al., 2017), and the first 30 PCAs were visualized using t-Distributed Stochastic Neighbor Embedding (t-SNE, *Rtsne* package) with a perplexity of 200 and learning rate of 100. Using the *FindClusters* function in *Seurat*, graph-based clustering was performed to cluster cells according to their gene expression profile (clustering resolution = 0.8, k-nearest neighbors = 18). See Table S1 for details. Clusters were annotated based on the expression of canonical marker genes, including *Fxyd2* and *Chchd10* (cancer cells), *Pecam1* and *Cdh5* (vascular ECs), *Cd3g* and *Cd3e* (T cells), *Nkg7* and *Gzma* (NK cells), *Cd79a* and *Cd79b* (B cells), *Ctss* (macrophages and monocytes), *Ccl17* (dendritic cells), *S100a9* and *S100a8* (neutrophils), *Mgp* and *Bgn* (mesenchymal cells), *Sftpa1* and *Sftpc* (pneumocytes). All cell clusters were used for downstream analysis.

Cluster identification

For each phenotype separately (ECs and mesenchymal cells from the EC-enriched dataset, and cancer cells, ECs, lymphocytes, myeloid cells, mesenchymal cells and pneumocytes from the non-EC-enriched dataset), we identified highly variable genes using the *Seurat FindVariableGenes* (for settings see Table S1), performed PCA on highly variable genes, followed by t-SNE visualization. To estimate the number of distinct cell subtypes with discriminating gene expression patterns, we used an in-house developed tool to color-code t-SNE plots for all detected genes, to empirically define the clustering resolution for each phenotype. Next, we applied graph-based clustering as implemented in the FindClusters function in Seurat (for settings see Table S1). Clusters were visualized using t-SNE to verify that all visually identified clusters were captured. Clusters with highly similar expression patterns indicative for representing the same biological subtype were merged into a single cluster.

Marker gene analysis

We identified top-ranking marker genes for each cell subtype by performing pairwise differential analysis of all clusters against all other clusters separately, using the *limma* package (version 3.34.9) (Ritchie et al., 2015). The results of each differential analysis were ordered based on the log$_2$ fold change (the most upregulated genes received the lowest rank number (top-ranking marker genes) and the most downregulated genes received the highest rank number). We obtained a final ranked marker gene list for each cluster by calculating the rank product for all genes in all pairwise comparisons. To assess statistical significance, we used a recently developed algorithm to determine p values for each marker gene based on the rank product statistic (Heskes et al., 2014), and obtained Benjamini-Hochberg adjusted pvalues using the R package *q-value* (Storey et al., 2015). We also quantified, for each marker gene, the fraction of cells in each cluster that expressed the marker gene above the population average and the average expression levels.

Cluster annotation

Clusters were annotated based on literature-curated marker genes of cell phenotypes. In case of an entirely unknown cell subtype or previously unrecognized sublineages of a canonical cell subtype, which could not be annotated based on canonical marker genes or gene sets, we used a three-step approach to identify a putative biological function. First, we searched through the top 50 ranking list of markers for a coherent set of genes involved in similar biological processes. Second, if we identified a putative signature (e.g., stress, invasion, etc.), we determined whether other genes associated with such a signature were also highest expressed in this phenotype. Third, we integrated insights from additional analysis (e.g., color-coded t-SNEs, heatmap analysis) into our assessment. Lowly sequenced clusters or clusters that could not be unambiguously assigned to a biologically meaningful phenotype might represent low quality cells or doublets and were excluded from the analysis. Batch effect correction of the dataset containing all pooled ECs (*in silico* selected from experiment 1 (enriched) and 2 (non-enriched), see Figure S2F–SH) was performed using *mnnCorrect,* as described above.

Data visualization

The R implementation of the Plotly software (https://github.com/ropensci/plotly) was used for t-SNE, violin plot and bar graph visualization. The *Heatmaply* R package (version 0.15.2) (Galili et al., 2018) was used for heatmap visualization. All heatmaps were based on cluster-averaged gene expression to account for cell-to-cell transcriptomic stochastics, and data was auto-scaled for visualization.

Gene ontology analysis

To identify GO terms that are over-represented in angiogenic pericytes, we performed pairwise differential gene expression analysis for the angiogenic pericyte cluster versus the quiescent co-opted pericyte cluster, using the *limma* package (version 3.34.9) (Ritchie et al., 2015). The top 100 genes from the resulting ranked list (sorted by $\log_2$ fold change) was used for gene ontology analysis using the Gorilla web tool using default settings (Eden et al., 2009).

Gene set enrichment analysis

We used gene set enrichment analysis (GSEA) as implemented in the *clusterProfiler* package (version 3.6.0) to compare metabolic gene expression signatures between angiogenic and quiescent pericytes and gene expression signatures in the hypoxic cancer cells. Gene set analysis was performed using gene sets from the Molecular Signatures Database (MSigDB version 5.2 downloaded from http://bioinf.wehi.edu.au/software/MSigDB/), a collection of expert annotated gene sets, and gene sets from the cancer single-cell state atlas (CancerSEA, http://biocc.hrbmu.edu.cn/CancerSEA/). GSEA scores were calculated for sets with a minimum of 5 detected genes, all other parameters were default.

Gene set variation analysis

We used Gene Set Variation Analysis (GSVA) using a collection of expert annotated vascular-related gene sets from the Molecular Signatures Database (MSigDB version 5.2 from http://bioinf.wehi.edu.au/software/MSigDB/), curated gene sets of lung EC phenotypes (Kalucka et al., 2020), a curated gene set of activated pericytes (Table S5) and the gene sets from the cancer single-cell state atlas (CancerSEA, http://biocc.hrbmu.edu.cn/CancerSEA/) to identify pathways and cellular processes enriched in different tissues. GSVA was performed as implemented in the *GSVA* R-package (version 1.26.0; default parameters) (Hänzelmann et al., 2013), where the gene-by-cell matrix is converted into a gene-set-by-cell matrix. GSVA scores were calculated for sets with a minimum of 5 detected genes, all other parameters were default. As cells can be sensitive to dissociation-induced artifacts, we also performed GSVA to identify cells strongly expressing a published dissociation gene signature (van den Brink et al., 2017). Clusters in which this signature was detected were removed if no other marker genes that could biologically explain a stress response were expressed.

Jaccard similarity analysis

To assess similarity of the pericyte phenotypes (within the mesenchymal cells) in the five different conditions (healthy lung, d10 & d21 untreated, d21 & d36 sunitinib-treated), we calculated similarity of marker gene sets using pairwise Jaccard similarity coefficients for all mesenchymal cell clusters per condition. The Jaccard similarity coefficient is defined as the size of the intersection divided by the size of the union of sets:

$$J(A,B) = \frac{|A \cap B|}{|A \cup B|} = \frac{|A \cap B|}{|A| + |B| - |A| \cap |B|}$$

Where J is the Jaccard index and A and B are two sets of marker genes (Levandowksy and Winter, 1971).

Meta-analysis of pericytes from published transcriptomics data

We performed a GSVA analysis with angiogenic and quiescent pericyte signatures on selected pericytes from previously published transcriptomic datasets. Briefly, we screened for murine lung scRNA-seq studies and identified four studies comprising three healthy lung studies and one lung tumor study. For datasets from Tabula Muris Consortium et al. (2018), Cohen et al. (2018)); Vanlandewijck et al. (2018); and He et al. (2018b), raw data extracted from GEO (GSE119228, GSE99235, GSE109774) and further processed as described above. We selected pericytes based on the simultaneous expression of *Pdgfrb* and *Mcam*, pooled the data, performed batch correction using *mnnCorrect* available from the *scran* package (Haghverdi et al., 2018) with a neighborhood size, k, of 50, identified highly variable genes using the *Seurat FindVariableGenes* function (mean lower threshold = 0.045, mean higher threshold = 8, dispersion threshold = 0.5), auto-scaled the data, summarized it by principal component analysis (PCA) using the *flash*PCA package (Abraham et al., 2017), and visualized the first 8 PCAs using t-Distributed Stochastic Neighbor Embedding (t-SNE, *Rtsne* package [van der Maaten and Hinton, 2008]) with a perplexity of 60 and learning rate of 100. Using the *FindClusters* function in *Seurat*, graph-based clustering was performed to cluster cells according to their gene expression profile (clustering resolution = 1, k-nearest neighbors = 15). See Table S1 for details. Next, we performed GSVA with gene sets containing the top 50 defining marker genes of the angiogenic and the quiescent pericyte cluster. We applied GSVA as implemented in the *GSVA* R-package (version 1.26.0; default parameters) (Hänzelmann et al., 2013), where the gene-by-cell matrix is converted into a gene-set-by-cell matrix. GSVA scores were calculated for sets with a minimum of 5 detected genes, all other parameters were default.

Ligand-receptor interaction analysis

To investigate potential interactomes in our data, we used the Python implementation of *CellPhoneDB* (Efremova et al., 2020). As input to the algorithm, we used a pooled normalized count matrix containing all cells from the repeat cohort, in which mouse gene names were converted to human orthologs using the *biomaRt* package (version 2.42.1). The following parameters were used for the analysis: data = hgnc_symbol; iterations = 1,000; threshold = 0.25.

QUANTIFICATION AND STATISTICAL ANALYSIS

Statistical analyses

To assess statistical significance for the top 50 marker genes for all phenotypes (Table S2), we used a recently developed algorithm to determine p values for each marker gene based on the rank product statistic (Heskes et al., 2014), and obtained Benjamini-Hochberg adjusted p values using the R package *qvalue* (Storey et al., 2015). For hierarchical clustering and bootstrap analysis, we first compiled the highly variable genes or top 50 marker genes of each cluster into a marker list. We calculated the mean of these marker genes and applied hierarchical clustering with Euclidean distance and complete linkage. The confidence of each branch of the tree was estimated by the bootstrap resampling approach from the R-package *pvclust* (Suzuki and Shimodaira, 2006), using a p value cutoff of 0.05. RNAscope data are representative tumor sections of n = 3 mice. A t test was used for all pairwise comparisons, ANOVA with the appropriate posthoc test for multiple group comparisons. Statistical details about each experiment can be found in the figure legends.

Software

All software is freely or commercially available and is listed in the STAR Methods description and Key resources table.